Received: 15 January 2024 | Revised: 16 April 2024 | Accepted: 6 May 2024

DOI: 10.1002/hbm.26720

RESEARCH ARTICLE

WILEY

EEG/MEG source imaging of deep brain activity within the maximum entropy on the mean framework: Simulations and validation in epilepsy

Jawata Afnan[1,2,3] | Zhengchen Cai[3] | Jean-Marc Lina[4,5,6] | Chifaou Abdallah[1,2,7] | Edouard Delaire[8] | Tamir Avigdor[1,2,7] | Victoria Ros[3] | Tanguy Hedrich[1] | Nicolas von Ellenrieder[3] | Eliane Kobayashi[3] | Birgit Frauscher[3,7] | Jean Gotman[3] | Christophe Grova[1,3,4,8]

[1]Multimodal Functional Imaging Lab, Biomedical Engineering Department, McGill University, Montréal, Québec, Canada

[2]Integrated Program in Neuroscience, McGill University, Montréal, Québec, Canada

[3]Montreal Neurological Institute, Department of Neurology and Neurosurgery, McGill University, Montréal, Québec, Canada

[4]Physnum Team, Centre De Recherches Mathématiques, Montréal, Québec, Canada

[5]Electrical Engineering Department, École De Technologie Supérieure, Montréal, Québec, Canada

[6]Center for Advanced Research in Sleep Medicine, Sacré-Coeur Hospital, Montréal, Québec, Canada

[7]Analytical Neurophysiology Lab, Department of Neurology, Duke University School of Medicine, Durham, North Carolina, USA

[8]Multimodal Functional Imaging Lab, Department of Physics and Concordia School of Health, Concordia University, Montréal, Québec, Canada

Correspondence
Christophe Grova, Multimodal Functional Imaging Lab, Biomedical Engineering Department, McGill University, Montréal, Québec, H3A 2B4, Canada.
Email: christophe.grova@concordia.ca

Funding information
Canadian Open Neuroscience Platform; Fonds de Recherche du Québec - Santé; Fonds de recherche du Québec - Nature et technologies; Canadian Institutes of Health Research, Grant/Award Numbers: FDN 143208, PJT-159948, PJT-175056

Abstract

Electro/Magneto-EncephaloGraphy (EEG/MEG) source imaging (EMSI) of epileptic activity from deep generators is often challenging due to the higher sensitivity of EEG/MEG to superficial regions and to the spatial configuration of subcortical structures. We previously demonstrated the ability of the coherent Maximum Entropy on the Mean (cMEM) method to accurately localize the superficial cortical generators and their spatial extent. Here, we propose a depth-weighted adaptation of cMEM to localize deep generators more accurately. These methods were evaluated using realistic MEG/high-density EEG (HD-EEG) simulations of epileptic activity and actual MEG/HD-EEG recordings from patients with focal epilepsy. We incorporated depth-weighting within the MEM framework to compensate for its preference for superficial generators. We also included a mesh of both hippocampi, as an additional deep structure in the source model. We generated 5400 realistic simulations of interictal epileptic discharges for MEG and HD-EEG involving a wide range of spatial extents and signal-to-noise ratio (SNR) levels, before investigating EMSI on clinical HD-EEG in 16 patients and MEG in 14 patients. Clinical interictal epileptic discharges were marked by visual inspection. We applied three EMSI methods: cMEM, depth-weighted cMEM and depth-weighted minimum norm estimate (MNE). The ground

truth was defined as the true simulated generator or as a drawn region based on clinical information available for patients. For deep sources, depth-weighted cMEM improved the localization when compared to cMEM and depth-weighted MNE, whereas depth-weighted cMEM did not deteriorate localization accuracy for superficial regions. For patients' data, we observed improvement in localization for deep sources, especially for the patients with mesial temporal epilepsy, for which cMEM failed to reconstruct the initial generator in the hippocampus. Depth weighting was more crucial for MEG (gradiometers) than for HD-EEG. Similar findings were found when considering depth weighting for the wavelet extension of MEM. In conclusion, depth-weighted cMEM improved the localization of deep sources without or with minimal deterioration of the localization of the superficial sources. This was demonstrated using extensive simulations with MEG and HD-EEG and clinical MEG and HD-EEG for epilepsy patients.

KEYWORDS
deep brain activity, epilepsy, HD-EEG, MEG, source imaging

Practitioner Points

- Proposed depth-weighted Maximum Entropy on the Mean (MEM) methods for EEG/MEG source imaging.
- Evaluation using realistic EEG/MEG simulations and actual EEG/MEG recordings from patients with focal epilepsy.
- Improvement in source reconstruction especially for deep sources in low SNR environment compared to standard MEM and depth-weighted MNE.

1 | INTRODUCTION

In addition to seizures, patients with epilepsy present interictal epileptic discharges (IED), characterized by spontaneous abnormal neuronal discharges usually generated from regions overlapping with the regions generating seizures (Hauf et al., 2012), but without clinical manifestation. IEDs occur more frequently than seizures and the localization of IED generators is crucial during the pre-surgical evaluation of patients with drug-resistant epilepsy (Bautista et al., 1999; Hufnagel et al., 2000).

Electro/Magneto- EncephaloGraphy (EEG/MEG) are widely used non-invasive techniques to detect IEDs and delineate the seizure onset zone and irritative zone (Rosenow & Lüders, 2001). The ability of EEG/MEG to detect deep brain activity is often debated, especially for MEG (Barkley & Baumgartner, 2003; Kaiboriboon et al., 2010; Leijten et al., 2003; Rampp & Stefan, 2007; Shigeto et al., 2002). Detection and localization of deep subcortical sources by EEG/MEG is challenging for several reasons: (i) rapid attenuation of the signals generated from deep structures as a function of the distance of the generator to the EEG/MEG sensors, which is more pronounced for MEG when considering gradiometers (Barkley & Baumgartner, 2003; Malmivuo & Plonsey, 1995). (ii) 'closed field' structure of the subcortical regions such that the generators cancel each other (Lorente De Nó, 1947; Murakami & Okada, 2006) and are difficult to detect by distant sensors and (iii) signals from deep structures propagate rapidly to the lateral cortex resulting in the superposition of the low signal to noise ratio (SNR) signals from deep structures and high SNR signals from superficial regions; this makes it difficult to disentangle those sources (Attal & Schwartz, 2013; Benar et al., 2021). This is especially true for mesial temporal lobe epilepsy, a common type of epilepsy where the IEDs generated in mesial temporal regions propagate to neocortical temporal regions with a 10 to 50 ms delay (Merlet & Gotman, 1999). However, compelling evidence is available now suggesting that deep brain activity can be recorded by EEG (Seeber et al., 2019) and MEG (Alberto et al., 2021; Kaiboriboon et al., 2010), as demonstrated by simultaneously recorded intracranial EEG (Dalal et al., 2009; Koessler et al., 2015; Pizzo et al., 2019).

The spatiotemporal localization of underlying neuronal generators from EEG/MEG sensors, called EEG/MEG source imaging (EMSI), is an ill-posed inverse problem. Solving the ill-posed EMSI problem requires making assumptions (constraints added for regularization), which vary for different methods. Minimum-norm estimate (MNE) is a widely used EMSI method (Hämäläinen & Ilmoniemi, 1994) choosing the solution that best fits the sensor data with a minimum overall energy of brain activity. As the amplitude of electrical potentials or magnetic fields decreases with the square of the distance from generators to sensors, EEG and MEG sensors have a higher sensitivity to superficial compared to deep generators (Heller & van Hulsteyn, 1992). Because of the constraint of minimum energy, standard MNE solutions have natural preferences toward localizing activity in superficial sources for which the sensors are more sensitive (Jeffs et al., 1987; Uutela et al., 1999), resulting in an underestimation

of deep sources. A depth-weighted version of MNE was proposed (Fuchs et al., 1999; Jeffs et al., 1987; Lin et al., 2006) to improve the accuracy of source localization for deep sources, by weighting the covariance structure of the source to allow enhancing activity from deep generators. In parallel, two noise-normalized versions of MNE have been proposed, dynamic statistical parametric mapping (dSPM) (Dale et al., 2000) and standardized low-resolution electromagnetic tomography (sLORETA) (Pascual-Marqui, 2002). These noise-normalized versions of MNE also allow for enhancing the contribution of deep sources when solving the EMSI problem (Lin et al., 2006). Exploiting the depth-weighted and noise-normalized versions of MNE, while using a realistic anatomical and electrophysiological model of deep brain activity, Attal and Schwartz (2013) showed that signals from subcortical sources can be detected by MEG with good accuracy, especially when considering single source activation. The localization from subcortical regions becomes more challenging when a cortical source is simultaneously active. In Attal and Schwartz (2013), for accurate localization, the simulated subcortical activity had an energy SNR of 20 (amplitude SNR of ~4.5 or 13 dB), which roughly corresponds to an evoked cortical MEG response obtained after averaging ~100 to 200 trials. In a low SNR scenario, which is usually the case for single events generated from deep structures, EEG/MEG source localization remains quite challenging. In addition, to study deep brain activity, an interesting anatomical and electrophysiological model was proposed by Attal et al. (2009) and Attal and Schwartz (2013). Depending on the types of neural generators (open and closed field cells) and their preferred orientation, subcortical structures were modeled as volume grids or surface meshes. The thalamus, striatum, and amygdala were modeled by placing current dipoles on the volume grid with random orientation; the hippocampus was modeled as a surface mesh placing the current dipoles orthogonally to the surface (similar to cortical source space) (Attal & Schwartz, 2013; Meyer et al., 2017).

In the context of epilepsy, recovering the spatial extent of the generator is also of importance in addition to localizing its origin. It has been reported that the generators of IEDs often are associated with a large area of cortex, for instance with a minimum area of 4–8 cm^2 for EEG (Ebersole, 1997; Merlet & Gotman, 1999; Tao et al., 2007; Von Ellenrieder et al., 2014) and 3–4 cm^2 for MEG (Hari, 1990; Mikuni et al., 1997; Oishi et al., 2002). The Maximum Entropy on the Mean (MEM) is an EMSI technique that can accurately localize the superficial generators together with their spatial extent, which we previously demonstrated for coherent MEM (cMEM), the standard variant of MEM, assuming a stable parcellation of the brain along time in the prior model and which is ideal for localization of epileptic spikes (Abdallah et al., 2022; Chowdhury et al., 2013, 2016; Grova et al., 2006). Our team also developed the wavelet MEM (wMEM) which is another variant of MEM, designed to localize the oscillatory components by transforming the data in the time-frequency domain before applying MEM localization (Afnan et al., 2023; Lina et al., 2012). In the present study, we propose a depth-weighted extension of cMEM and wMEM, following the depth-weighted strategy implemented by Cai et al. (2022) to reconstruct functional Near-InfraRed Spectroscopy data. We also added the hippocampus as a surface mesh in our source model, as proposed by Attal et al. (2009). Our objective is to demonstrate the ability of depth-weighted MEM methods to localize deep generators accurately while largely retaining their ability to localize superficial generators. We considered high-density EEG (HD-EEG) and MEG realistic simulations of single-source epileptic activity (Chowdhury et al., 2013; Grova et al., 2006) as well as more complex scenarios involving epileptic activity in the hippocampus and neocortical regions. The mixed sources scenario was generated to mimic IEDs in mesial temporal lobe epilepsy characterized by initial mesial activity followed by propagated neocortical activity (Merlet & Gotman, 1999). Finally, we evaluated the performance of depth-weighted MEM methods with IEDs recorded from HD-EEG and MEG in patients with focal epilepsy for whom the presumed localization of the focus was defined as a region along the cortical surface (including the hippocampus) using all available information from presurgical evaluation.

2 | MATERIALS AND METHODS

2.1 | Experimental design

The analysis pipeline is summarized in Figure 1. We propose depth-weighting in cMEM implementation (Section 2.2). The depth-weighted cMEM was first evaluated using realistic simulations of IED on MEG and HD-EEG (Section 2.3), before localizing actual IEDs from MEG, and HD-EEG (Section 2.4) from patients with drug-resistant focal epilepsy. The proposed method was compared with standard cMEM and depth-weighted MNE. We included a surface of both hippocampi, as an additional deep structure in the source model (Section 2.5).

2.2 | Maximum entropy on the mean method and depth weighting

The EEG/MEG inverse problem was solved using the Maximum Entropy on the Mean (MEM) (Amblard et al., 2004; Chowdhury et al., 2013). The key feature of this method is that it relies on a flexible spatial prior, assuming that brain activity is organized in cortical parcels. The activity of every parcel is scaled by the probability of activation of every parcel, which is tuned through a hidden state variable. When the parcel is active, a Gaussian distribution is used as the prior of the activity within the parcel. When the parcel is inactive, a Dirac distribution is considered that allows to shut down the activity from this parcel. Starting from such a prior "reference" distribution, the model is fitted to data by maximizing the relative entropy between the solution and the prior. As a result, MEM can either switch off or switch on the parcels during the localization process, while still allowing local contrast on the cortical surface within the active parcels. MEM provides accurate localization of the generators together with their spatial extent, as demonstrated by the standard variant of MEM, cMEM (Abdallah et al., 2022; Chowdhury et al., 2013; Chowdhury

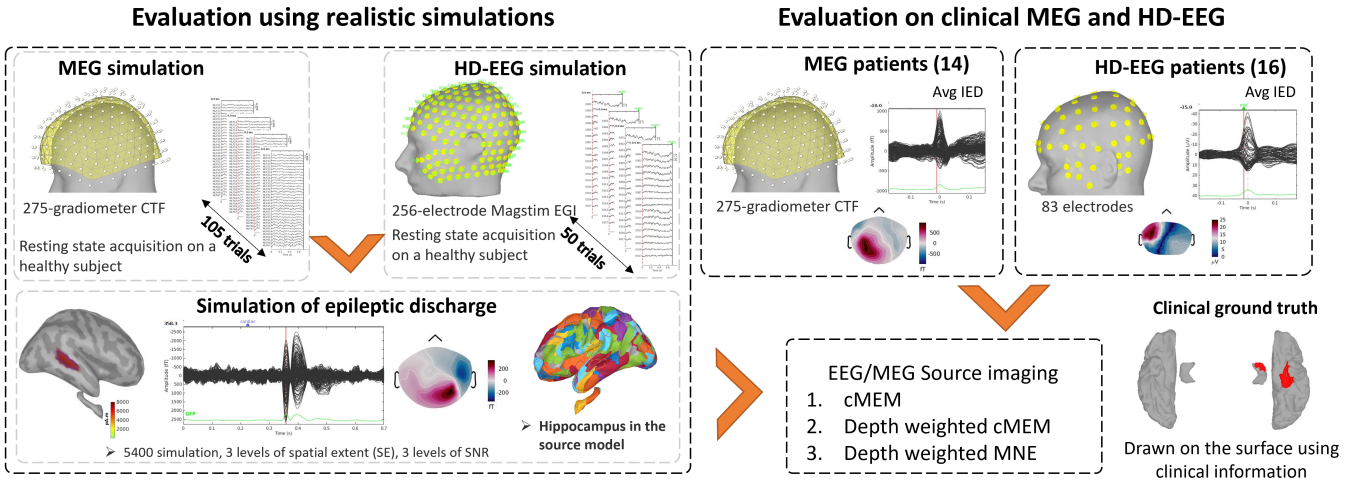

FIGURE 1 Analysis pipeline to evaluate depth-weighted cMEM compared to standard cMEM and depth-weighted MNE using MEG and HD-EEG simulations of epileptic discharges, as well as actual interictal epileptic discharges from MEG and HD-EEG in patients with focal epilepsy.

et al., 2016; Grova et al., 2016), as well as the wavelet-based extension, wMEM (Lina et al., 2012; Pellegrino et al., 2016; von Ellenrieder et al., 2016). For coherent MEM (cMEM), the term "coherent" refers to the fact that we are using a coherent spatial prior, that is, a data driven parcellation which is fixed along time (Abdallah et al., 2022; Chowdhury et al., 2013; Chowdhury et al., 2016; Grova et al., 2016). wMEM consists in applying first a discrete wavelet transformation (Daubechies wavelets) to characterize the oscillatory patterns in the data before considering the MEM solver to solve the EMSI problem (Lina et al., 2012). cMEM and wMEM implementations are available in the BrainEntropy plugin of Brainstorm software (Tadel et al., 2011) (https://neuroimage.usc.edu/brainstorm/Tutorials/TutBEst/).

cMEM/wMEM for EMSI have a preference toward superficial solutions (Afnan et al., 2023; Grova et al., 2006), since so far, we have not considered any depth-weighted strategy for both methods. On the other hand, depth weighted strategy is commonly considered for MNE (Hämäläinen & Ilmoniemi, 1994) and Beamformer (Van Veen et al., 1997). To solve the EMSI inverse problem for each source location, the uncertainty of the activity of the underlying sources is modeled by the source covariance matrix. Deeper sources tend to have greater uncertainty in EMSI, resulting in higher values in the covariance matrix compared to superficial sources. Therefore, an a priori source covariance matrix should appropriately account for the variance differences across source locations. To do so, the diagonal of the source covariance can be weighted by the forward model of each source, quantifying the influence of source depth of each source at a specific power ω. This standard approach is used as a default implementation of depth-weighted MNE (Fuchs et al., 1999; Lin et al., 2006). A similar depth-weighted strategy was implemented within the cMEM framework by Cai et al. (2022) for the reconstruction of functional Near-InfraRed Spectroscopy data. We weighted the source covariance for each parcel when generating the spatial prior (see additional details in the Appendix A). The depth weighting parameter was set to $\omega = 0.5$ as this is also used as a default value for depth-weighted MNE implemented in Brainstorm. We also investigated the depth weighting parameter ω for a range of values: $\omega = 0.1$, 0.3, 0.5, 0.7, and 0.9. The results are presented in the Data S1.

Here, we evaluated the newly proposed depth-weighted cMEM ($cMEM_\omega$, ω being the depth weighting factor) and compared with original cMEM (not depth-weighted) and depth-weighted MNE (MNE_ω) using first simulated IEDs (Section 2.3) and then actual IEDs from MEG and HD-EEG (Section 2.4). To calculate the noise covariance, we used 2 s of resting state data from each subject. For MNE_ω, we estimated the regularization hypermeter λ by using the SNR of the data, as $\lambda = 1/SNR^2$, with the SNR set to 3 (default value in Brainstorm).

We applied a similar depth weighting strategy for wMEM and validated it using the same dataset of simulated IEDs. Since wMEM considers discrete wavelets and is designed to localize oscillatory components of the signals, IEDs signals might not be ideal for validation of wMEM. However, our focus was on the improvement of depth-weighted wMEM ($wMEM_\omega$) compared to original wMEM, not on the comparison between wMEM and cMEM. We compared $wMEM_\omega$ with cMEM, wMEM, $cMEM_\omega$, and MNE_ω in Section 3.5 and Data S1. However, since this study focuses mainly on cMEM and $cMEM_\omega$, the wMEM results are reported in Supplementary Data S1.

2.3 | MEG and HD-EEG realistic simulations

2.3.1 | Realistic simulation parameters

The realistic simulation framework was developed by adding simulated epileptic activity to a real MEG or HD-EEG resting state background (Chowdhury et al., 2016; Grova et al., 2006; Lina et al., 2012) using the following steps: (i) the time course of an interictal epileptic spike was modeled with three gamma functions for each vertex within a specific generator defined along the cortical surface; (ii) the simulated time courses of the generator defined in the source space were

multiplied by the forward model to obtain sensor level data (more details in Chowdhury et al. (2013) and Grova et al. (2006)); (iii) the simulated sensor level data was finally superimposed on real resting state MEG or HD-EEG background obtained from a healthy subject. The maximum amplitude of each vertex of the simulated source was set to 2.85 nA.m. This value has been chosen to mimic the realistic amplitude of a typical epileptic spike. In each simulation, one trial of background HD-EEG/MEG was used, thus mimicking the occurrence of a single non-averaged epileptic spike. The simulations were prepared separately for MEG and HD-EEG using resting state data and head models obtained from two different healthy subjects.

The spatial extent (SE) of the generator was obtained by expanding the region around a randomly chosen location (called the seed) in a geodesic manner on the cortical surface (or hippocampus surface), using different spatial neighborhood order. The actual SNR of the simulated sensor signal was defined as the ratio of maximum activity at the peak of the simulated epileptic activity to the standard deviation estimated within 300 ms background activity for the channel exhibiting this peak (Equation 1).

$$\mathrm{SNR\,(dB)} = 20log_{10}\frac{|\text{maximum activity at the peak}|}{\text{standard deviation for 300 ms background}} \quad (1)$$

Depending on the location and spatial extent of the generator, the SNR of the sensor-level signal varied, although the signal strength of the generators for each vertex was kept equal to $S_0 = 2.85$ nA.m at the peak of the simulated spikes. In other words, the SNR of the simulations varied depending on the location, spatial extent and orientation of the sources. As expected, it was higher for the superficial sources and lower for the deep sources and resulted in relatively realistic SNR expected at the sensor level (see Figures S1 and S2 for actual sensor level SNR of the simulated signals).

Simulation of a single epileptic source: For each modality (MEG/HD-EEG), we generated 2700 simulations for three levels of the spatial extent (i.e., spatial neighborhood order around the seed) of the generators (SE = 2 [$\sim$5 cm^2], 3 [$\sim$10 cm^2], 4 [20 cm^2]), and three levels of source amplitude strength ($2S_0$, $3S_0$, $4S_0$ where $S_0 = 2.85$ nA.m), while keeping the amplitude of sensor level background at the same level. Since changing source amplitude strength directly impacted SNR at the sensor level, for simplification purposes, we denoted these three levels of source strengths as the SNR of 2, 3, 4 in this document. For each combination of SE and SNR, 300 simulations were performed where the location of each generator was selected randomly on the cortical or hippocampal surfaces. The proportion of simulated generators involving the hippocampus for each combination was 2.2 ± 0.8% for MEG and 1.9 ± 0.3% for HD-EEG. The resulting sensor level SNRs of those hippocampal generators were 11.3 ± 4.09 dB for MEG and 18 ± 4.6 dB for HD-EEG. In Figure S3, we showed all the single hippocampal sources generated among the total 300 MEG simulations, considering one combination of SE and SNR (SE3 SNR2). We also reported the amplitude of the sensor exhibiting the highest amplitude and the corresponding sensor-level SNR. In addition, Figure S4 illustrates the decomposition of the simulated signals into the simulated spike and the MEG background for two examples in Figure S3.

Simulation of the mixture of cortical and hippocampal sources in MEG: We also simulated 100 sets of epileptic activity on MEG, involving a mixture of two generators, one in the hippocampus and the other in the lateral temporal cortex with a 15 ms delay. These simulations mimicked typical epileptic discharges in a mesial temporal epilepsy case, where the signal is generated in the hippocampus and rapidly propagates to the lateral part of the temporal cortex (Merlet & Gotman, 1999). The seeds were chosen randomly but restricted to the hippocampus and the ipsilateral temporal cortex. Unlike the single source simulations in the hippocampus (low SNR), we generated higher SNR signals in the hippocampus for this set by increasing the number of vertices in the hippocampus (see Section 2.5). The resulting sensor level SNR of the simulated signals was 14 ± 4.3 dB for the hippocampal generators and 20 ± 5.4 dB for the cortical generators. The average spatial extent was $\sim$6 cm^2 for hippocampal sources and $\sim$10 cm^2 for cortical sources.

2.3.2 | Resting-state data acquisition for simulation

The resting state MEG and HD-EEG trials were acquired from two different healthy subjects (Hedrich et al., 2017). These studies were approved by the Research Ethics Board of the Montreal Neurological Institute and Hospital and a written informed consent was signed by all participants before the procedures. MEG: We acquired MEG in a magnetically shielded room at the MEG center of the Montreal Neurological Institute (MNI) using a 275-channel CTF system (MISL, Vancouver, Canada) with a sampling rate of 1200 Hz. The participant was seated and instructed to keep eyes open. Continuous head localization was obtained using three localization coils attached to the nasion and left and right peri-auricular points on each subject. The exact position of the localization coils, as well as the shape of the head of the subject, were digitized with a 3D Polhemus localizer for subsequent coregistration with the anatomical MRI. The co-registration was done using the skin surface segmented from a high-resolution T1-weighted MRI acquired on the same subject at the MRI center of the MNI. The iterative closest point algorithm implemented in Brainstorm (Tadel et al., 2019) was used to ensure accurate coregistration between the skin mesh segmented from the MRI and the head shape digitized using the 3D Polhemus localizer, to estimate a rigid transformation matrix (3 rotations, 3 translations). HD-EEG: HD-EEG was recorded using a 256-electrode EGI system (Magstim Electrical Geodesics Inc., Eugene, OR) with a sampling rate of 1000 Hz. A high-resolution T1-weighted MRI was acquired on the same subject using the scanner located at the MNI. Co-registration was done using individual T1 MRI and EEG sensor positions estimated using the Geodesic Photogrammetry System (GPS, Electrical Geodesic Inc., Eugene, OR) (Hedrich et al., 2017). The same coregistration approach employed for MEG was applied to HD-EEG and MRI.

2.3.3 | Data preprocessing

The selected data were investigated to remove artifacts from eye blinks and muscle activity. Cardiac artifact and eye movement artifacts were removed from HD-EEG and MEG using Signal Space Projection method (Uusitalo & Ilmoniemi, 1997). The preprocessing included applying a bandpass filter between 0.3 and 70 Hz, a notch filter at 60 Hz, noisy channels removal, and downsampling to 600 Hz. For MEG, the third-order gradient compensation was also applied. A total of 105 segments each lasting 0.7 s were extracted from the clean MEG data. A total of 50 segments of 0.7 s were extracted from the clean HD-EEG data. These segments were selected to be added as background realistic noise to simulated epileptic spikes.

2.4 | IEDs from patients with focal epilepsy

For patients' data, both MEG and HD-EEG studies were approved by the Research Ethics Board of the Montreal Neurological Institute and Hospital and a written informed consent was signed by all participants before the procedures.

MEG: MEG from 14 patients with focal epilepsy (7 F; mean age, 31.4 ± 11.0 Y, 8 mesial temporal) were acquired in supine position on the same 275-channel CTF system as mentioned in Section 2.3.2 at 1200 Hz sampling rate. MEG data were acquired between 2008 and 2018 for presurgical evaluation (see Table S1). We included patients for whom at least five IEDs were marked by visual inspection and enough clinical information was available to estimate a reasonable ground truth (by C.A and V. R). MEG was performed with the patient lying down in a supine position, lasting ∼1 h (10 runs of 6 min each). HD-EEG: The HD-EEG patient cohort included 16 patients (7 F; mean age, 33.6 ± 10.9 Y, 9 mesial temporal) with drug-resistant focal epilepsy who underwent 24–48 h long HD-EEG recordings (83 electrodes, sampling 1000 Hz) during presurgical evaluation at the MNI epilepsy unit between 2019 and 2022 (see Table S2). The HD-EEG dataset was part of another study published by our group (Avigdor et al., 2024). HD-EEG was performed using the Nihon Koden system (Tokyo, Japan) using 83 collodion glued electrodes (10-10 EEG system). Note that we used a different HD-EEG system (256-electrode Magstim EGI system) for recording background activity from healthy participants. Co-registration for MEG and HD-EEG with corresponding anatomical MRI was done as described in Section 2.3.2. Preprocessing of data included: bandpass filtered between 0.3 and 70 Hz, notch filter at 60 Hz, downsampling to 600 Hz and removal of channels with artifacts by visual inspection. EEG data were analyzed using average reference montage.

Marking of IEDs and clinical ground truth: IEDs were visually marked by a board-certified epileptologist (MEG: C.A. and V.R., HD-EEG: C.A and B.F.). The number of IEDs marked for each patient is summarized in Tables S1 and S2. We analyzed the average IED for each patient, considering a 200 ms window around the peak of the IED. To quantify the accuracy of source imaging, the presumed clinical ground truth for each patient was drawn as a region on the cortical surface (including the hippocampus) using all clinical information available from presurgical evaluation with long-term video EEG monitoring, anatomical MRI, fluorodeoxyglucose-positron emission tomography, neuropsychological evaluation, intracranial EEG results or surgical cavity drawn using pre- and post-surgical MRI for patients who became seizure-free (for MEG), varying based on the availability of the information. Our evaluation was therefore performed based on a semi-quantitative definition of the presumed ground truth, as reported in our previous studies (Pellegrino et al., 2018; Pellegrino, Xu, et al., 2020).

2.5 | Source space and forward model estimation

Brain segmentation and reconstruction of the white/gray matter interface for the cortex were obtained using recon-all from FreeSurfer software package (Dale et al., 1999). The subcortical structures were also segmented using FreeSurfer. The subsequent analysis to create the source model and forward model was conducted in Brainstorm (Tadel et al., 2011). We considered the cortical mesh of the middle layer which is equidistant from the white matter and pial surfaces consisting of ∼300,000 vertices. We included the two hippocampi from the subcortical structures. Each hippocampus consisted of ∼3000–4000 vertices (depending on the subject anatomy). For both the cortex and the hippocampus, the sources were located on the surface of the structures with a fixed orientation orthogonal to the surface at each point. Then we merged the cortical and hippocampal surfaces and downsampled the source space to ∼8000 vertices. This resulted in ∼4 vertices/cm^2 on the cortical and the hippocampal surface. A uniform density of vertices was used for both surfaces for simulations of single source generators and patients' data. Only for the simulations of mixed sources in MEG (Section 2.3.1), we used a source model where the density of vertices was double in the hippocampus (∼8 vertices/cm^2). The reason was to generate higher SNR simulations in the hippocampus while keeping other simulation parameters similar compared to single source simulations. Once our source space was defined, the forward model was computed using OpenMEEG software using a 3-layer Boundary Element model (BEM) (Kybic et al., 2005) consisting of brain, skull, and scalp surfaces with conductivity values of 0.33, 0.0165, and 0.33 S m^{-1}, respectively (Zhang et al., 2006).

2.6 | Validation metrics

The performance of three source imaging methods (cMEM, cMEM$_\omega$, and MNE$_\omega$) was assessed using the following three validation metrics: (i) Area Under the ROC Curve (AUC): A detection accuracy index to assess the sensitivity to the spatial extent of the sources in the context of distributed sources model (adapted by Grova et al. (2006) for the specific problem of EMSI validation while allowing unbiased estimates, more details provided in Chowdhury et al. (2013)). (ii) D_{min}: the minimum distance localization error was the Euclidean distance in mm

from the maximum of the map to the closest vertex belonging to the ground truth. When this maximum was located inside the simulated source, D_{min} was set to 0 mm (Hedrich et al., 2017). (iii) Spatial dispersion (SD): the SD metric measured the spatial spread (in mm) of the localization around the Ground Truth. To estimate SD, we considered the root mean square of the square of the distance from the estimated source to the ground truth weighted by the energy of the source localization map at each vertex (Hedrich et al., 2017). For each IED, we estimated those metrics at the peak of the IEDs for simulations, and at the midpoint of the rising spike for patients' averaged IEDs. We assessed AUC, SD, and D_{min} of each simulated source as a function of the eccentricity of the source, defined as the mean of the distance between all the vertices in the ground truth and the center of the head. Deep sources have therefore low eccentricity and superficial sources have high eccentricity. We applied the non-parametric Friedman test to compare the three source imaging methods (Durbin-Conover test for pair-wise comparisons, p value corrected for multiple comparisons using Bonferroni). Similar analyses were also performed to evaluate wMEM and wMEM$_\omega$ methods, results are reported in the Data S1.

3 | RESULTS

3.1 | Simulation of single epileptic source: MEG

Figure 2 summarizes the performance of our three validation metrics—AUC, SD, and D_{min} for cMEM, cMEM$_\omega$, and MNE$_\omega$ estimated for 300 MEG simulations with spatial extent SE = 3 (11.8 ± 2.1 cm^2) and SNR = 2 (11.6 ± 5.4 dB). Figure 2d shows the average eccentricity values for those 300 generators. In Figure 2, the metrics are shown as colormap for 300 generators, where all the vertices within a generator are represented by one color associated with the value of the corresponding metric. The AUC values were overall improved when considering cMEM$_\omega$ in comparison to cMEM, especially in mesial regions. cMEM$_\omega$ performances in terms of SD and D_{min} were also improved in deeper regions when compared to cMEM. Both cMEM and cMEM$_\omega$ exhibited smaller SD values when compared to MNE$_\omega$.

The improvement in localization for deep sources by cMEM$_\omega$ compared to cMEM is more clearly presented in Figure 3, which illustrates that cMEM$_\omega$ improved the localization mostly on the medial side (deep sources) without or with minimal worsening of the localization in the lateral and superficial regions. The statistical comparisons for these maps are presented in Figure 4 for deep sources and Figure S5 for superficial sources.

Figure 4a presents the detailed distributions of validation metrics AUC, SD, and D_{min} as a function of eccentricity for the 300 MEG simulations shown in Figures 2 and 3. Similar to Figure 3, Figure 4 shows that the localization improved for regions with low eccentricity (0–60 mm, deep sources). We compared the metrics for cMEM$_\omega$, cMEM and MNE$_\omega$ for regions with eccentricity <60 mm (Figure 4b1, b2, b3). The localization for those regions was significantly improved by cMEM$_\omega$ compared to cMEM in terms of AUC, SD and D_{min} (p < .001, AUC$_{cMEM\omega\text{-}cMEM}$: 0.14 ± 0.11, SD$_{cMEM\text{-}cMEM\omega}$: 3.9 ± 2.8 mm, Dmin$_{cMEM\text{-}cMEM\omega}$: 3.1 ± 3.3 mm), the effect being reported as median ± median absolute deviation of the difference between cMEM$_\omega$ and cMEM. Compared to MNE$_\omega$, the localization was also significantly improved by cMEM$_\omega$ in terms of AUC and SD (p < .001, AUC$_{cMEM\omega\text{-}MNE\omega}$: 0.11 ± 0.07, SD$_{MNE\omega\text{-}cMEM\omega}$ 19.5 ± 5.6 mm). D_{min} by cMEM$_\omega$ was also improved when compared to MNE$_\omega$ but did not pass the significance threshold (Dmin$_{MNE\omega\text{-}cMEM\omega}$: 0.3 ± 7.6 mm).

For regions with eccentricity >60 mm (Figure S5), the AUC and D_{min} for cMEM$_\omega$ were overall similar to cMEM (AUC$_{cMEM\omega\text{-}cMEM}$: −0.01 ± 0.02, Dmin$_{cMEM\text{-}cMEM\omega}$: 0.0 ± 0.0 mm). The SD was slightly worsened by cMEM$_\omega$ when compared to cMEM (p < .001, SD$_{cMEM\text{-}cMEM\omega}$: −2.9 ± 1.8 mm). However, the SD was significantly improved by cMEM$_\omega$ compared to MNE$_\omega$ (p < .001, SD$_{MNE\omega\text{-}cMEM\omega}$: 23.8 ± 5.3 mm). In terms of SD, both cMEM and cMEM$_\omega$ were still largely significantly lower than MNE$_\omega$ (p < .001, SD$_{MNE\omega\text{-}cMEM}$: 26.0 ± 4.9 mm). The lowest median D_{min} was found for MNE$_\omega$, however, it was not significantly lower than cMEM$_\omega$. See also Figures S6–S16 for 2400 MEG simulations with other combinations of SE and SNR. Similar improvement by cMEM$_\omega$ was found compared to cMEM and MNE$_\omega$ for all combinations.

Figure S17 presents the distribution of AUC, SD, and D_{min} for 300 MEG simulations as a function of eccentricity for cMEM$_\omega$ for five different values of depth weighting parameter ω (ω = 0.1, 0.3, 0.5, 0.7, and 0.9). As ω increases, the localization accuracy for deep sources improves. However, for higher ω values, localization for superficial sources deteriorates, as observed in SD for ω = 0.7, 0.9, and in AUC, SD, and D_{min} for ω = 0.9.

3.2 | Simulation of mixed sources in the hippocampus and the neocortex in MEG

Figure 5 shows an example simulation of a complex or mixed source scenario, the first simulated generator is in the hippocampus (peak at 358 ms) and is followed by another generator along the lateral temporal cortex after a 15 ms delay (peak at 373 ms), mimicking a situation likely occurring in patients with mesial temporal lobe epilepsy. We calculated the metrics at 358 ms for the hippocampus and at 373 ms for the neocortex, considering the two sources are independent. We considered the whole cortex when estimating the metrics for both sources. For the hippocampal source, cMEM$_\omega$ localized the generator whereas cMEM failed, as reflected by AUC, SD and D_{min}. The metrics by cMEM and cMEM$_\omega$ were (cMEM/cMEM$_\omega$): AUC:0.38/0.74, SD: 25.9 mm/20.2 mm, D_{min}: 25.3 mm/24.9 mm. The metrics for MNE$_\omega$ for the hippocampal source were: AUC: 0.71, SD: 34.5 mm, D_{min}: 23.5 mm. For the superficial source at 373 ms, both cMEM and cMEM$_\omega$ localized the generator. The metrics for cMEM and cMEM$_\omega$ were (cMEM/cMEM$_\omega$): AUC:0.93/0.90, SD: 12.2 mm/15.3 mm, D_{min}: 0 mm/0 mm. The metrics for MNE$_\omega$ for the superficial source were: AUC: 0.81, SD: 28.8 mm, D_{min}: 0 mm.

Figure 6 summarizes the metrics for 100 simulations of mixed sources, following a complex scenario similar to the one illustrated

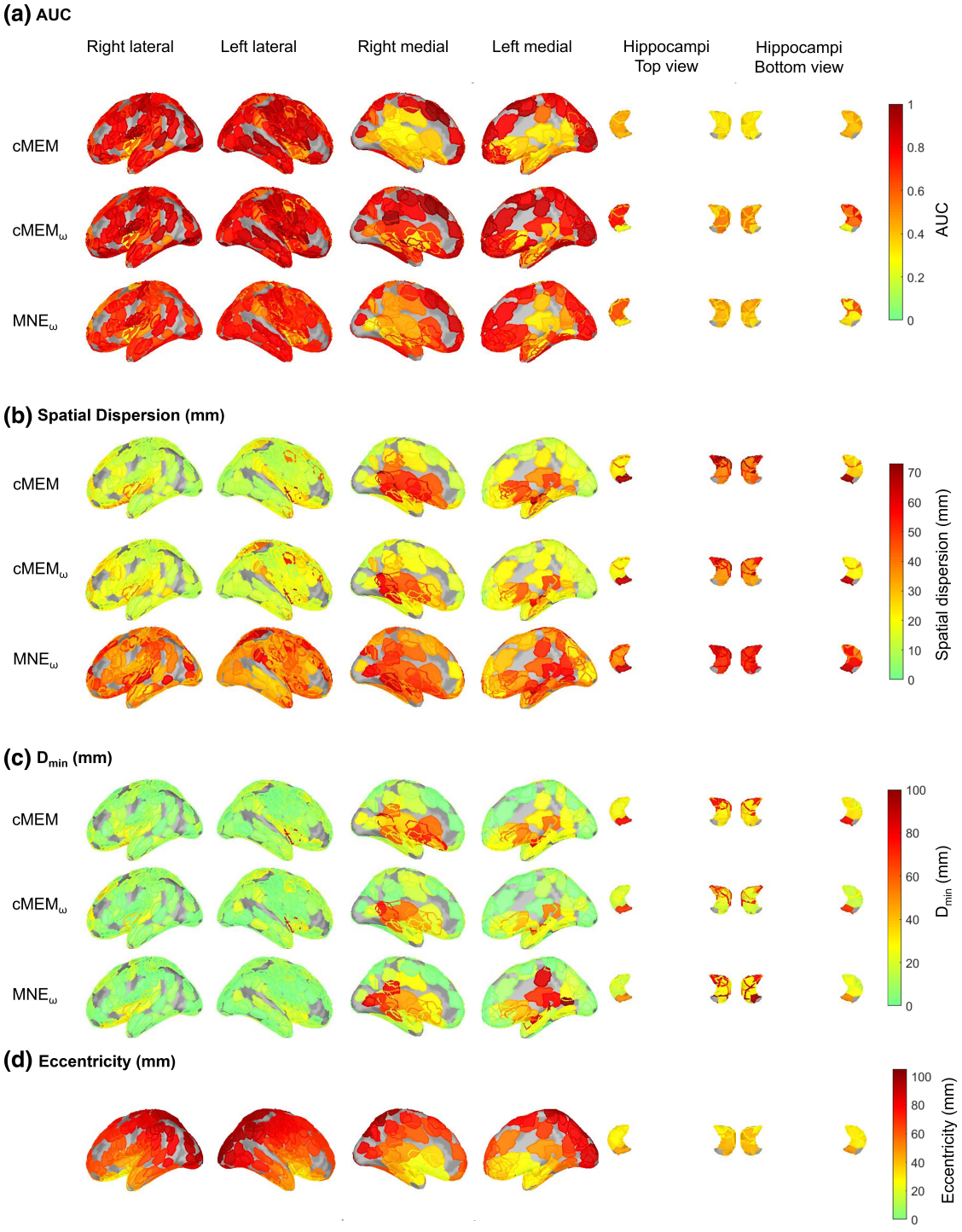

FIGURE 2 (a) AUC, (b) SD, and (c) D_{min} for three source imaging methods are shown on the cortical surface at the locations of 300 simulated sources in MEG. The average eccentricity values for those 300 generators are shown in (d). Each parcel is one simulated source with the color representing the metric value associated with it. Regions where no sources were generated are shown as grey. When there was overlap between sources, a line was superimposed on the new color to illustrate the overlap from the previous source. Increases in AUC and decreases in SD and D_{min} by $cMEM_{\omega}$ were observed mostly for the medial regions, whereas $cMEM_{\omega}$ and cMEM presented similar performances for superficial sources. Brain maps are shown for six views: right lateral, left lateral, right medial, left medial, hippocampi top, and hippocampi bottom.

in Figure 5. The first column shows the AUC, SD, and D_{min} at 358 ms for the source simulated in the hippocampus. AUC and SD were significantly improved by $cMEM_{\omega}$ compared to cMEM and MNE_{ω} ($p < .001$, $AUC_{cMEM\omega\text{-}cMEM}$: 0.26 ± 0.08, $AUC_{cMEM\omega\text{-}MNE\omega}$: 0.11 ± 0.09, $SD_{cMEM\text{-}cMEM\omega}$: 4.3 ± 2.6 mm, $SD_{MNE\omega\text{-}cMEM\omega}$: 17.6 ± 6.2 mm). D_{min} was significantly improved by $cMEM_{\omega}$ compared to

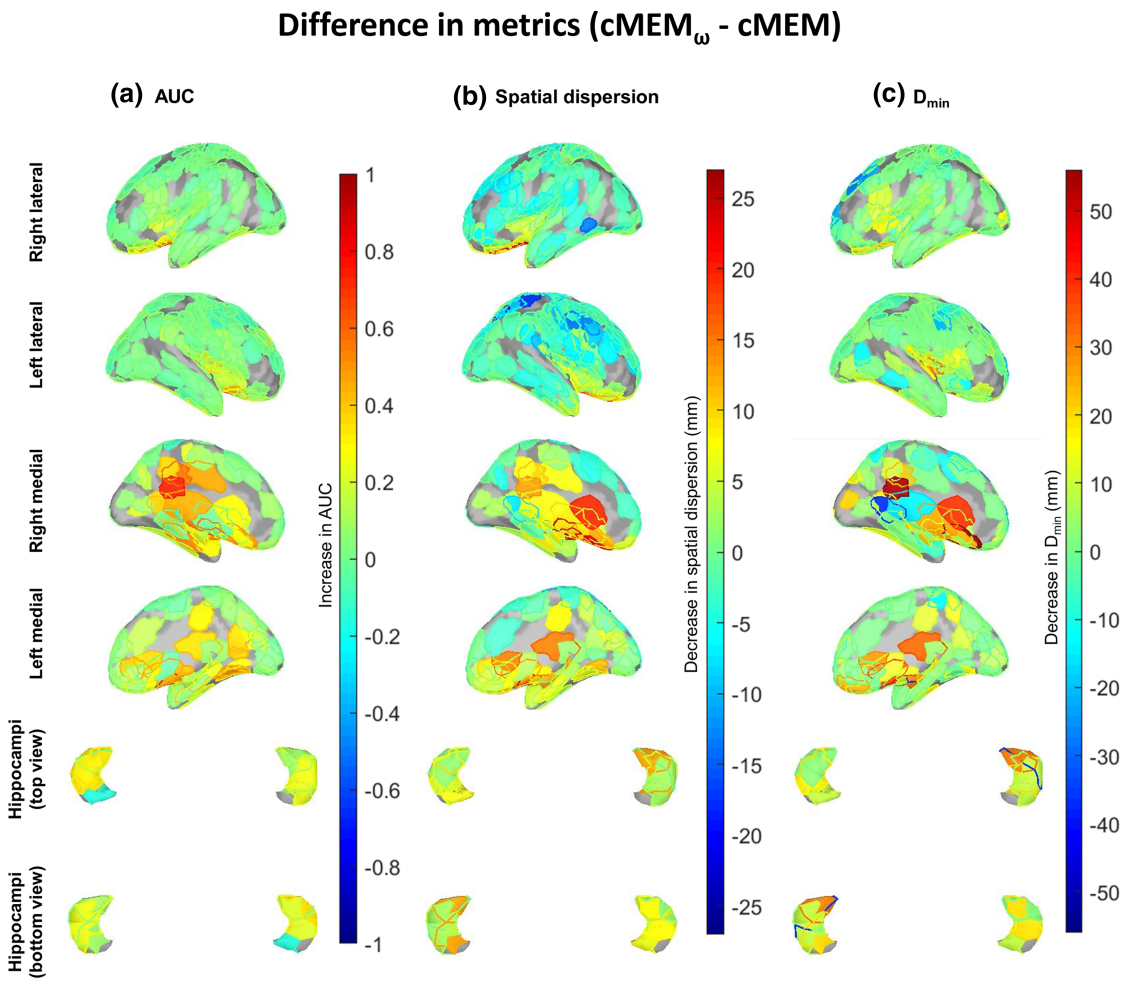

FIGURE 3 The differences in AUC, SD, and D_{min} between cMEM$_\omega$ and cMEM (cMEM$_\omega$ – cMEM) are shown on the cortical surface at the locations of 300 simulated sources in MEG. Increases in AUC and decreases in SD and D_{min} (warmer color) were observed mostly for the deeper regions. Regions where no sources were generated are shown as grey. When there was overlap between sources, a line was superimposed on the new color to illustrate the overlap from the previous source. Brain maps are shown for six views: right lateral, left lateral, right medial, left medial, hippocampi top, and hippocampi bottom.

cMEM ($p < .001$, Dmin$_{cMEM\text{-}cMEM\omega}$: 3.3 ± 3.3 mm). Compared to MNE$_\omega$, D_{min} was also significantly improved by cMEM$_\omega$ ($p < .05$, Dmin$_{MNE\omega\text{-}cMEM\omega}$: 5.2 ± 8.1 mm).

For the neocortical generator simulated at 373 ms, cMEM$_\omega$ showed similar AUC but slightly decreased SD compared to cMEM (AUC$_{cMEM\omega\text{-}cMEM}$: 0.01 ± 0.03, SD$_{cMEM\text{-}cMEM\omega}$: −1.7 ± 2.6 mm). Both cMEM and cMEM$_\omega$ showed improved AUC and SD compared to MNE$_\omega$ ($p < .001$, AUC$_{cMEM\omega\text{-}MNE\omega}$: 0.09 ± 0.05, AUC$_{cMEM\text{-}MNE\omega}$: 0.06 ± 0.06, SD$_{MNE\omega\text{-}cMEM\omega}$: 20.6 ± 5.1 mm, SD$_{MNE\omega\text{-}cMEM}$: 21.5 ± 5.3 mm). D_{min} was slightly improved in cMEM$_\omega$ compared to cMEM ($p < .01$, Dmin$_{cMEM\text{-}cMEM\omega}$: 0.0 ± 2.8 mm). Similar D_{min} was found for cMEM$_\omega$ and MNE$_\omega$ (Dmin$_{MNE\omega\text{-}cMEM\omega}$: 0.0 ± 3.7 mm).

3.3 | Simulation of single epileptic source: HD-EEG

Similar to the MEG results in Figure 3, Figure 7 shows the improvement in AUC, SD and D_{min} for 300 EEG simulations of epileptic activity (SE = 3, SNR = 2). The HD-EEG equivalent of Figure 2 is shown in Figure S18. Figure 7 illustrates that HD-EEG localization improved mostly on the medial side (deep sources) without or with minimal worsening of the localization in the lateral and superficial regions.

Figure 8 presents the metrics as a function of eccentricity for the 300 HD-EEG simulations (SE = 3 and SNR = 2), showing that the localization accuracy improved with cMEM$_\omega$ for regions with low eccentricity (deep sources, eccentricity <45 mm). The eccentricity threshold was chosen based on the results from 2700 HD-EEG simulations where the localization accuracy from cMEM and cMEM$_\omega$ started to converge at ∼45 mm, (Figures 8 and S19–S21). For MEG, this threshold was ∼60 mm. We summarized the results from cMEM, cMEM$_\omega$, and MNE$_\omega$ as boxplots for regions with eccentricity <45 mm (Figure 8) and regions with eccentricity >45 mm (Figure S22).

For sources with eccentricity <45 mm, the localization was significantly improved by cMEM$_\omega$ in terms of all three metrics compared to

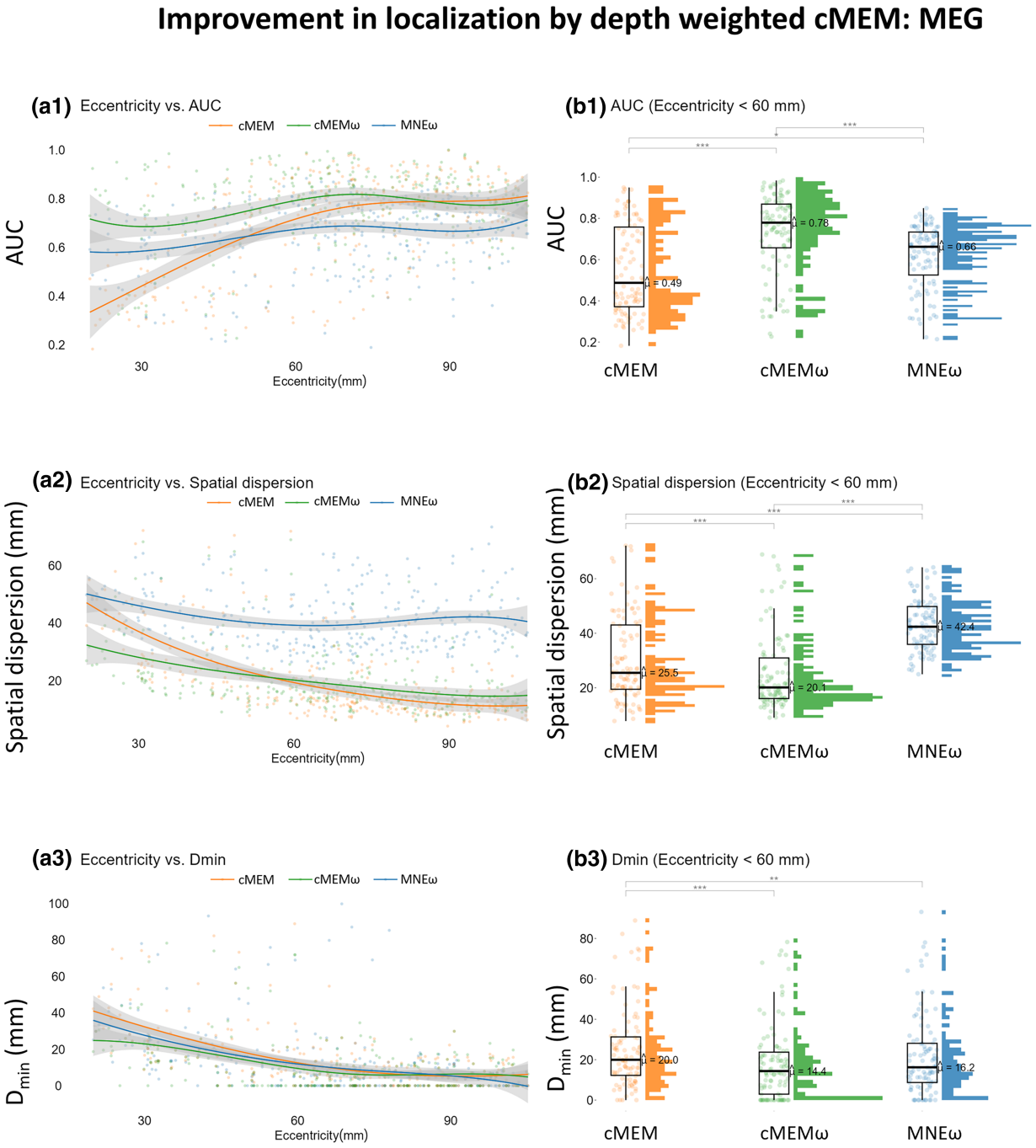

FIGURE 4 For 300 MEG simulations at SE = 3 and SNR = 2, the plot of AUC (a1), SD (a2), and D_{min} (a3) as a function of eccentricity for cMEM, cMEM$_\omega$ and MNE$_\omega$. The comparison of the three methods is summarized for AUC (b1), SD (b2), and D_{min} (b3) for 99 (out of 300) sources with an eccentricity of <60 mm. On each boxplot, the central mark indicates the median, and the bottom and top edges of the box indicate the 25th and 75th percentiles, respectively. If the groups are statistically different after post-hoc analysis, the significance levels are shown as: ***p < .001, **p < .01, and *p < .05.

cMEM (p < .001, $AUC_{cMEM\omega\text{-}cMEM}$: 0.05 ± 0.03, $SD_{cMEM\text{-}cMEM\omega}$: 2.4 ± 2.8 mm, $Dmin_{cMEM\text{-}cMEM\omega}$: 5.5 ± 5.0 mm) and MNE$_\omega$ (p < .001, $AUC_{cMEM\omega\text{-}MNE\omega}$: 0.20 ± 0.05, $SD_{MNE\omega\text{-}cMEM\omega}$: 17.1 ± 3.2 mm, $Dmin_{MNE\omega\text{-}cMEM\omega}$: 11.8 ± 10.0 mm).

For regions with eccentricity >45 mm (Figure S22), AUC and D_{min} for cMEM$_\omega$ were similar to cMEM ($AUC_{cMEM\omega\text{-}cMEM}$: 0.00 ± 0.02, $Dmin_{cMEM\text{-}cMEM\omega}$: 0 ± 0 mm). In terms of SD, cMEM$_\omega$ worsened slightly but significantly compared to cMEM (p < .001, $SD_{cMEM\text{-}cMEM\omega}$: −2.1 ± 1.1 mm). On the other hand, AUC and SD for cMEM$_\omega$ were significantly improved compared to MNE$_\omega$ (p < .001, $AUC_{cMEM\omega\text{-}MNE\omega}$: 0.13 ± 0.05, $SD_{MNE\omega\text{-}cMEM\omega}$: 13.3 ± 3.8 mm). Even if we observed slight worsening of cMEM$_\omega$ compared to cMEM for SD ($SD_{cMEM\text{-}cMEM\omega}$: −2.1 ± 1.1 mm), SD values remained low for both cMEM and cMEM$_\omega$ when compared to MNE$_\omega$ ($SD_{MNE\omega\text{-}cMEM}$: 15.2 ±

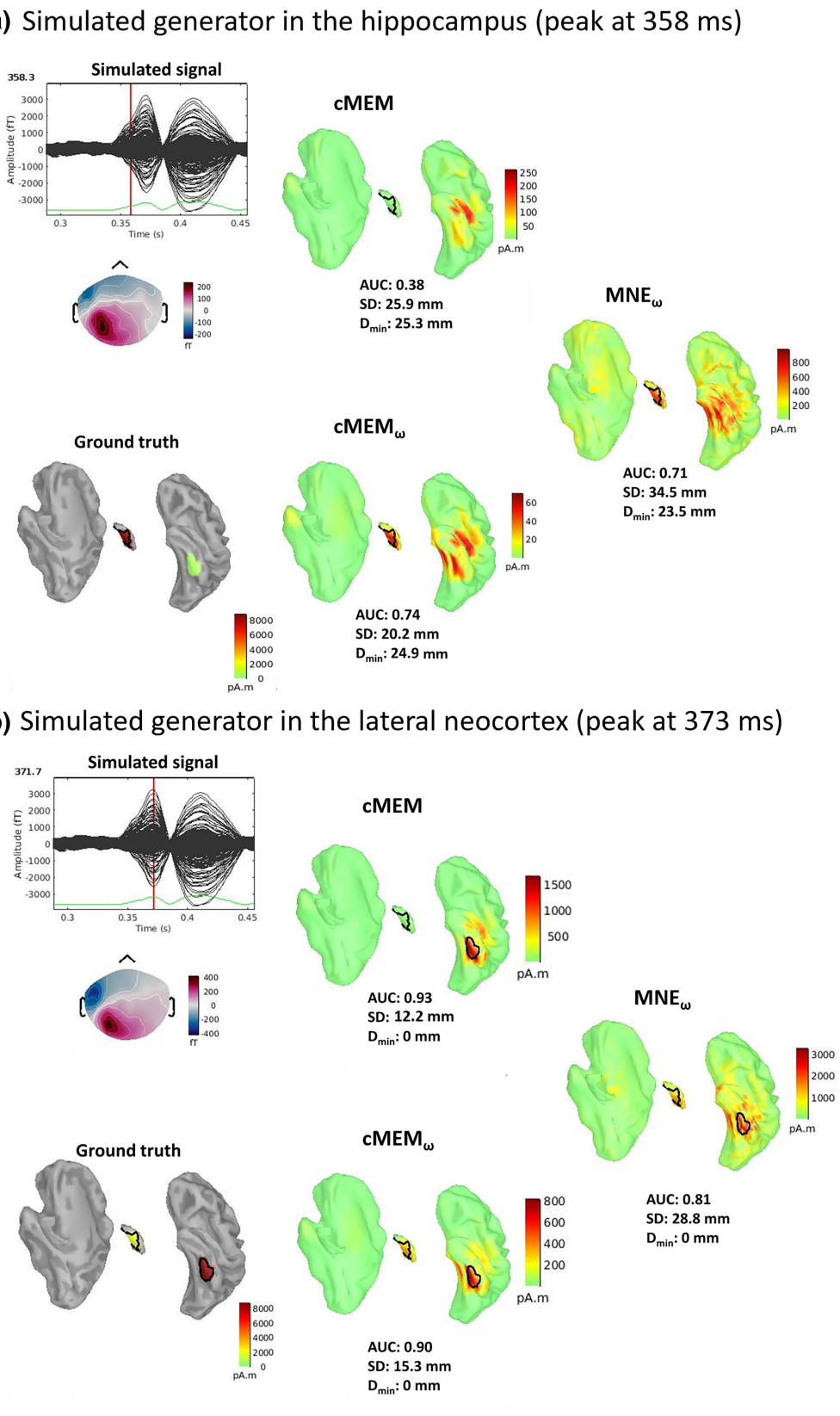

FIGURE 5 Example of two simulated generators first in the hippocampus (a) and then in the lateral neocortex after 15 ms delay (b). Three source imaging methods were applied to the averaged interictal epileptic discharges. The surface of the hippocampus is included in the source model (and presented in the figure as separate structures). The metrics AUC, SD, and D_{min} were calculated at 358 ms (peak of the source in the hippocampus) and at 373 ms (peak of the neocortical source). The scale is different for the three methods but source maps have been interpreted relatively for each method.

3.0 mm, $SD_{MNE\omega\text{-}cMEM\omega}$: 13.3 ± 3.8 mm). In terms of D_{min}, all three methods exhibited similar accuracy ($Dmin_{cMEM\text{-}cMEM\omega}$: 0.0 ± 0.0 mm, $Dmin_{MNE\omega\text{-}cMEM\omega}$: 0.0 ± 3.8 mm, $Dmin_{cMEM\text{-}MNE\omega}$: 0.0 ± 1.8 mm). See also Figures S23–S30 for 2400 HD-EEG simulations with other combinations of SE and SNR. Similar improvement by $cMEM_\omega$ was found compared to cMEM and MNE_ω for all combinations.

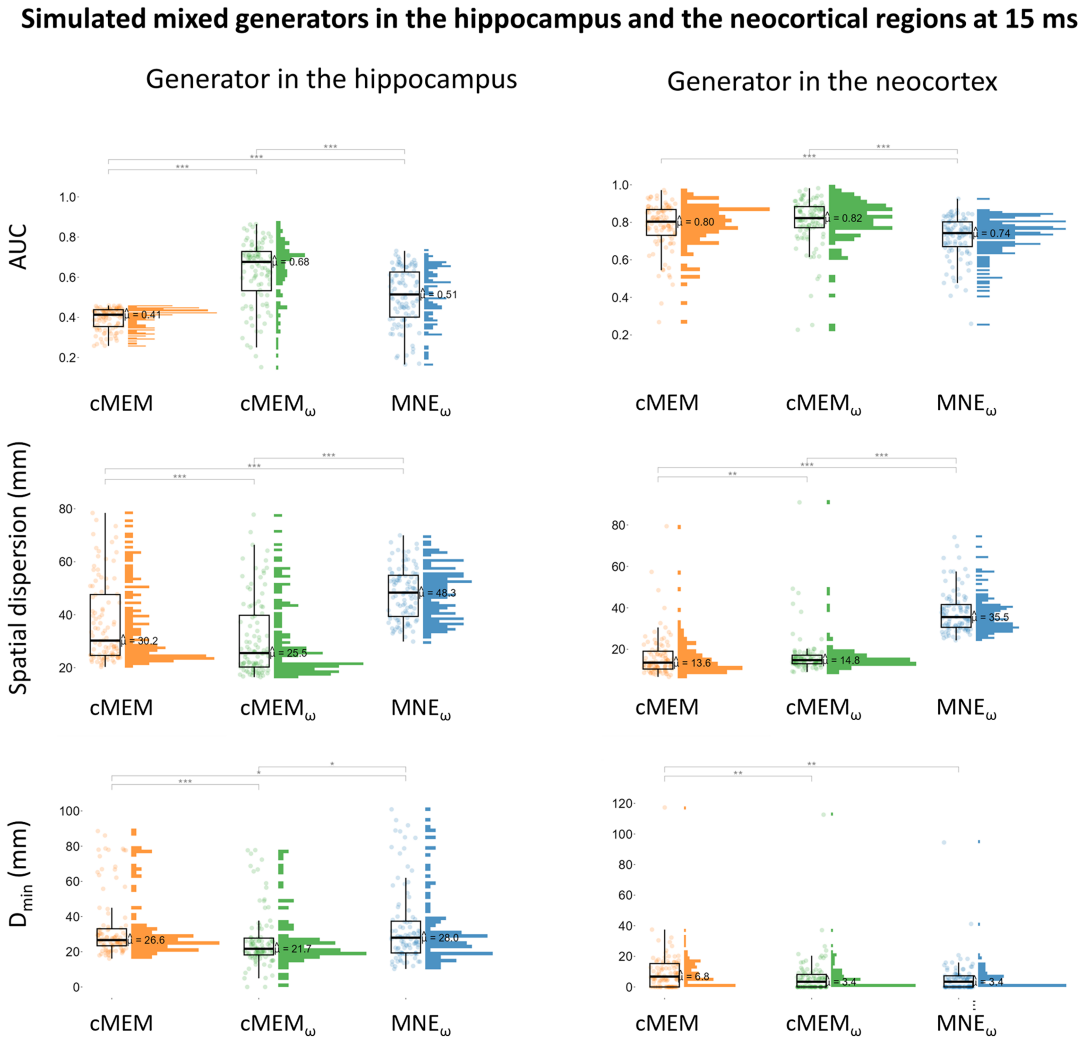

FIGURE 6 Source imaging for 100 simulations of mixed generators in the hippocampus and the ipsilateral neocortex after 15 ms delay. AUC, SD, and D_{min} are calculated separately for each generator at the peak of the spike (358 ms for hippocampal generator and 373 ms for neocortical generator). On each boxplot, the central mark indicates the median, and the bottom and top edges of the box indicate the 25th and 75th percentiles, respectively. If the groups are statistically different after post-hoc analysis, the significance levels are shown as: ***$p < .001$, **$p < .01$, and *$p < .05$.

3.4 | Evaluation on clinical MEG/HD-EEG data from patients with focal epilepsy

MEG: Figure 9a shows an example of MEG source localization for a patient with mesial temporal lobe epilepsy. The source imaging methods were applied on an averaged IED (number of IEDs: 16, sensor level SNR at the peak: 30 dB). The metrics were calculated at the midpoint of the rising phase of the spike (−10 ms, sensor level SNR at −10 ms: 26 dB). cMEM was not able to localize the underlying hippocampal generator, whereas the depth-weighted methods, $cMEM_\omega$ and MNE_ω could localize this deep generator during the rising phase of the averaged IED. The metrics for cMEM/$cMEM_\omega$ were: AUC: 0.43/0.79, SD: 21.7/16.6 mm and D_{min}: 18.3/10.6 mm. The results for MNE_ω were: AUC: 0.76, SD: 27.5 mm, D_{min}: 13.0 mm. All three methods mainly retrieved the propagated activity within temporal neocortical regions. Figure 9b compares the metrics for three source imaging methods in MEG for eight patients with mesial temporal lobe epilepsy, where the clinical ground truth involved the mesio-temporal structures including the hippocampus. The sensor level SNR of the averaged IEDs were 22.7 ± 6.6 dB at the peak and 20.33 ± 7.05 dB at the midpoint of the rising phase of the spike. The localization was significantly improved by $cMEM_\omega$ compared to cMEM in terms of AUC, SD ($AUC_{cMEM\omega\text{-}cMEM}$: 0.19 ± 0.04, $SD_{cMEM\text{-}cMEM\omega}$: 4.9 ± 0.3 mm, $p < .001$) and D_{min} ($Dmin_{cMEM\text{-}cMEM\omega}$: 7.6 ± 6.3 mm, $p < .05$). Compared to MNE_ω, $cMEM_\omega$ improved the localization significantly in terms of AUC ($p < .05$, $AUC_{cMEM\omega\text{-}MNE\omega}$: 0.13 ± 0.04) and SD ($p < .001$, $SD_{MNE\omega\text{-}cMEM\omega}$: 11.7 ± 1.7 mm). The median D_{min} was lower for $cMEM_\omega$ compared to MNE_ω ($Dmin_{MNE\omega\text{-}cMEM\omega}$: 0.0 ± 2.8 mm), but not statistically significant.

Figure S31a summarizes the metrics estimated for 14 patients including the mesial temporal cases and also other superficial cases. The sensor level SNR of the averaged IEDs were 24.0 ± 7.7 dB at the peak and 20.7 ± 7.4 dB at the midpoint of the rising phase of the spike. Overall improvement by $cMEM_\omega$ was observed compared

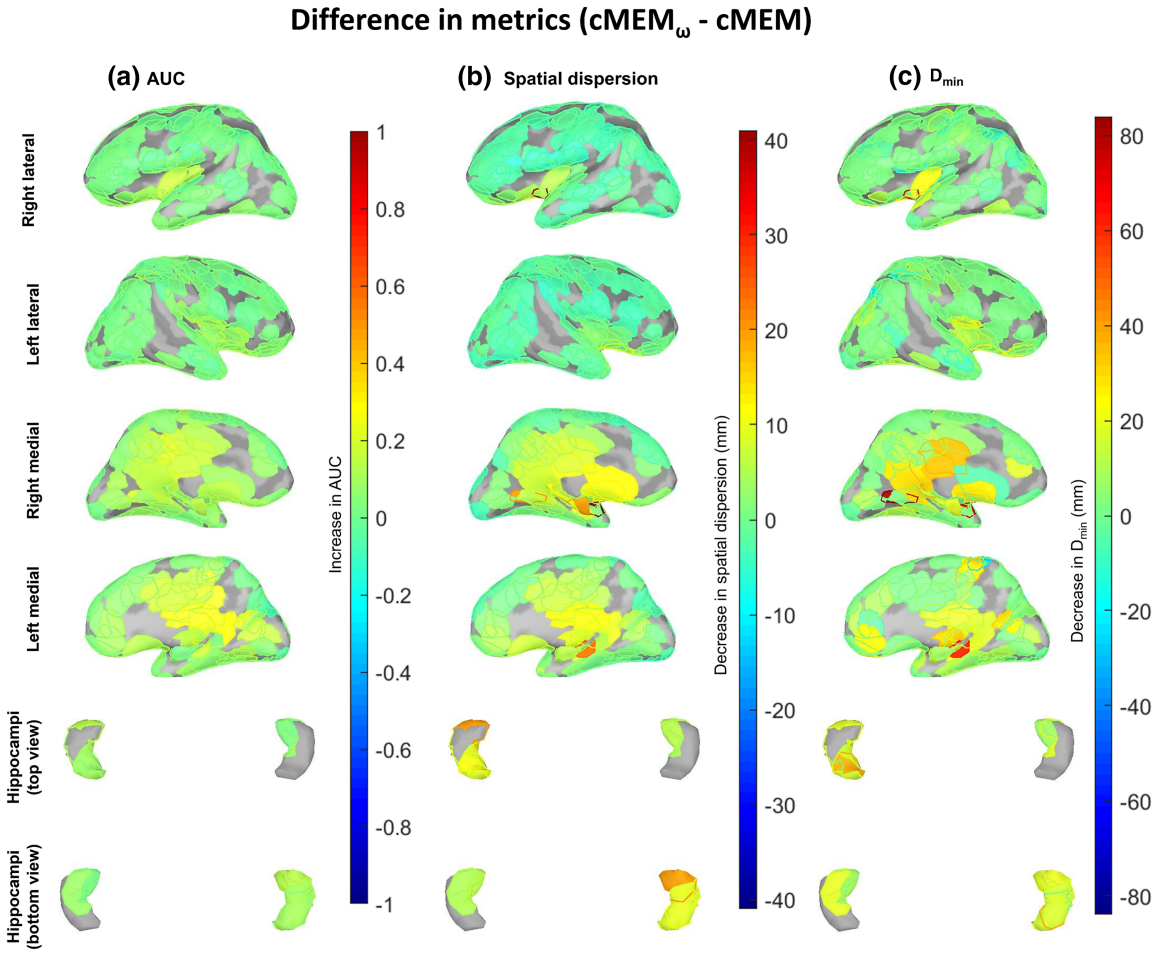

FIGURE 7 The differences in AUC, SD, and D_{min} between $cMEM_{\omega}$ and cMEM ($cMEM_{\omega}$ – cMEM) are shown on the cortical surface at the locations of 300 simulated sources in HD-EEG. Increases in AUC and decreases in SD and D_{min} (presented warmer color) were observed mostly for the deeper regions. Regions where no sources were generated are shown as grey. When there was overlap between sources, a line was superimposed on the new color to illustrate the overlap from the previous source. Brain maps are shown for six views: right lateral, left lateral, right medial, left medial, hippocampi top and hippocampi bottom.

to cMEM (not statistically significant). Compared to MNE_{ω}, $cMEM_{\omega}$ slightly improved the localization in terms of AUC (not statistically significant) and SD ($p < .001$). The lowest median of D_{min} was found for MNE_{ω} when compared to cMEM and $cMEM_{\omega}$. We also verified that the improvement brought by depth weighting was not dependent on the overall quality of the ground truth data, when comparing results between the seizure-free group and the other group for both MEG and HD-EEG data (see details in the Data S2).

HD-EEG: Figure 10a presents an example of HD-EEG source localization for a patient with mesial temporal lobe epilepsy. Unlike the MEG result shown in Figure 9a, cMEM could localize the hippocampal generator for HD-EEG. $cMEM_{\omega}$ improved the localization compared to cMEM in terms of AUC, SD and D_{min}. The metrics for cMEM/$cMEM_{\omega}$ were: AUC: 0.60/0.67, SD: 21.0/15.6 mm and D_{min}: 30/0 mm. The results for MNE_{ω} were: AUC: 0.36, SD: 47 mm, D_{min}: 30 mm.

Figure 10b shows the boxplots summarizing the metrics for cMEM, cMEMω and MNEω for nine patients with mesial temporal lobe epilepsy, for which the ground truth involved the mesio-temporal structures that include the hippocampus. The sensor level SNR of the averaged IEDs were 28.60 ± 4.95 dB at peak and 26.92 ± 5.88 dB at the midpoint of the rising phase of the spike. $cMEM_{\omega}$ significantly improved the localization compared to cMEM in terms of AUC ($p < .001$, $AUC_{cMEM\omega\text{-}cMEM}$: 0.04 ± 0.01) and SD ($SD_{cMEM\text{-}cMEM\omega}$: 2.9 ± 0.7 mm). D_{min} was also improved by $cMEM_{\omega}$ compared to cMEM ($Dmin_{cMEM\text{-}cMEM\omega}$: 0.4 ± 1.1 mm) but not statistically significant. Compared to MNE_{ω}, $cMEM_{\omega}$ provided improved AUC ($p < .001$, $AUC_{cMEM\omega\text{-}MNE\omega}$: 0.10 ± 0.03), SD ($p < .001$, $SD_{MNE\omega\text{-}cMEM\omega}$: 16.0 ± 3.2 mm) and slightly improved D_{min} ($Dmin_{MNE\omega\text{-}cMEM\omega}$: 3.2 ± 5.2 mm, not statistically significant).

Figure S31b summarizes the metrics for all 16 HD-EEG patients including mesial temporal cases and other extra-temporal cases. The sensor level SNR of the averaged IEDs were 28.09 ± 4.40 dB at the peak and 25.40 ± 5.00 dB at the midpoint of the rising phase of the spike. Overall improvement by $cMEM_{\omega}$ was observed compared to cMEM (not statistically significant). Compared to MNE_{ω}, $cMEM_{\omega}$ significantly improved the

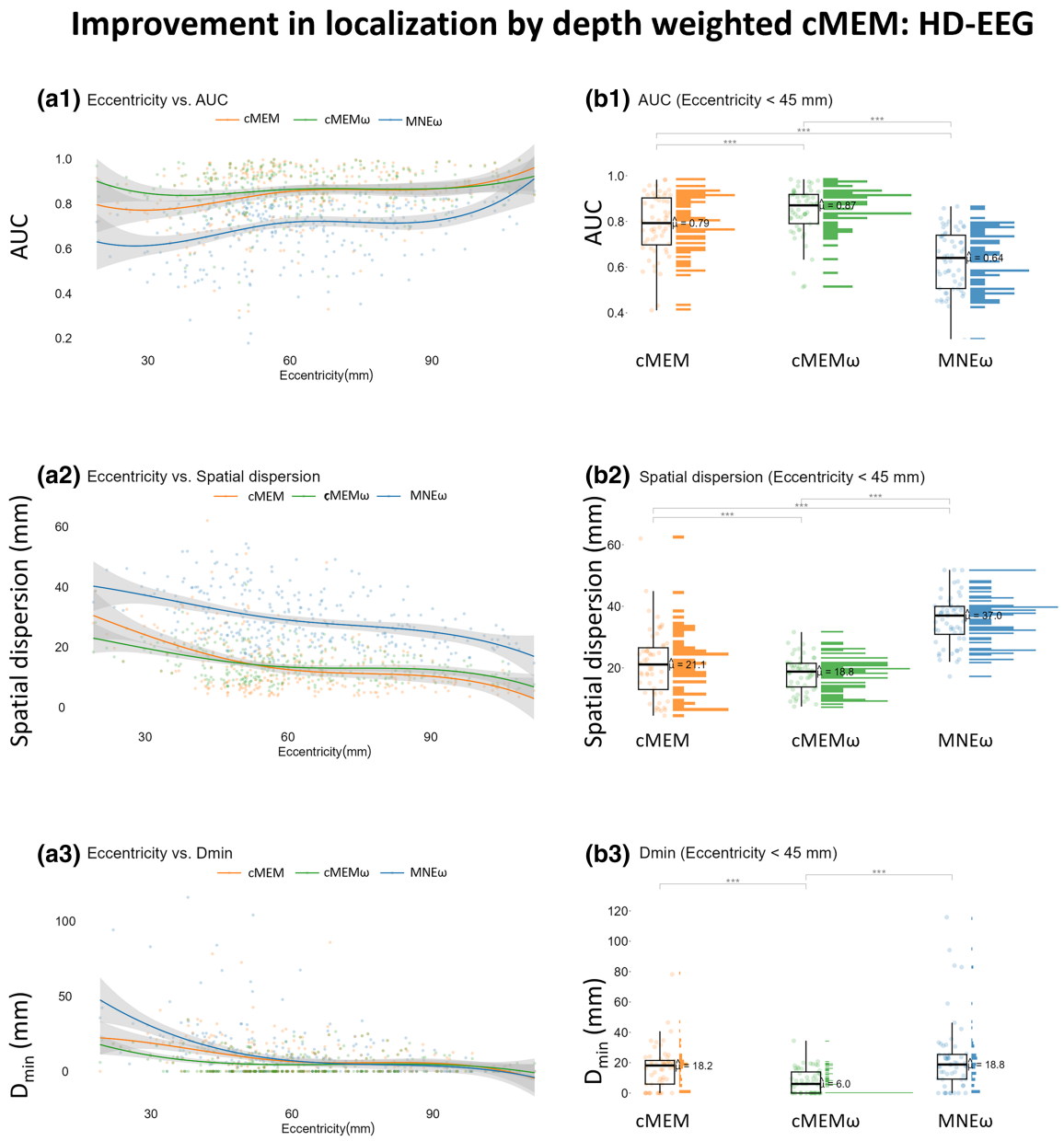

FIGURE 8 For 300 HD-EEG simulations at SE = 3 and SNR = 2, the plot of AUC (a1), SD (a2), and D_{min} (a3) as a function of eccentricity for three source imaging methods. The comparison of the three methods is summarized for AUC (b1), SD (b2), and D_{min} (b3) for 56 (out of 300) deep sources with an eccentricity <45 mm. For each boxplot, the central mark indicates the median, and the bottom and top edges of the box indicate the 25th and 75th percentiles, respectively. If the groups are statistically different after posthoc analysis, the significance levels are shown as: ***$p < 0.001$, **$p < 0.01$, and *$p < 0.05$.

localization in terms of AUC ($AUC_{cMEM\omega\text{-}MNE\omega}$: 0.11 ± 0.06), SD ($SD_{MNE\omega\text{-}cMEM\omega}$: 16.7 ± 6.0 mm) and D_{min} ($Dmin_{MNE\omega\text{-}cMEM\omega}$ 3.0 ± 9.0 mm).

3.5 | Depth-weighted wMEM

Similar to cMEM, depth weighting improved the localization for deep sources for wMEM method as well. Figure S32 shows the metrics AUC, SD and D_{min} as a function of eccentricity for the 300 MEG simulations presented in Figure 4, but also this time considers wMEM and its depth weighted implementation, $wMEM_{\omega}$. Overall, the findings for wMEM versus $wMEM_{\omega}$ were similar to cMEM versus $cMEM_{\omega}$. Detailed statistical comparisons are presented in the Supplementary material (section S1, Figures S32 and S33). We also provided wMEM results as a function of eccentricity for all combinations of SE and SNR levels for MEG simulations in Figures S34–S36 and HD-EEG simulations in Figures S37–S39. For all combinations of MEG and HD-EEG, similar trends were found as described in Figures S32 and S33. We decided not to provide detailed statistical comparisons for wMEM results for other combinations of HD-EEG and MEG simulations. Our results were overall similar to the ones reported in Figures S32 and

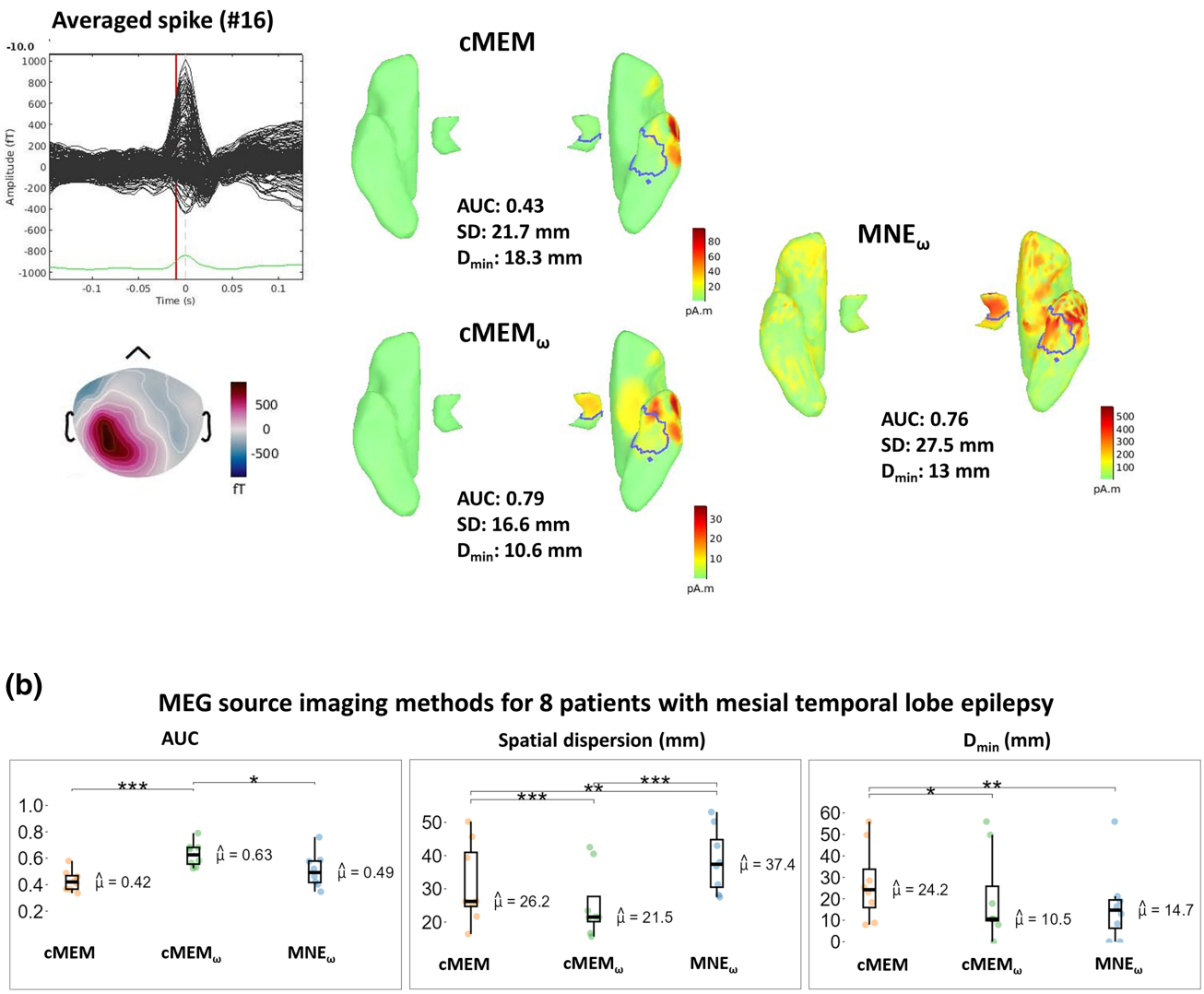

FIGURE 9 (a) Example of a MEG patient with mesial temporal lobe epilepsy. The source imaging methods were applied to the average of 16 selected interictal epileptic discharges. The surface of the hippocampus is included in the source model (shown as separate structures). The metrics AUC, SD, and D_{min} were calculated at the midpoint of the rising phase of the spike (−10 ms). The scale is different for the three methods, but source maps are interpreted relatively for each method. (b) Comparison of the MEG source imaging methods in terms of the validation metrics AUC, SD and D_{min} for eight patients with mesial temporal lobe epilepsy. Each boxplot represents metrics from one source imaging method. On each boxplot, the central mark indicates the median, and the bottom and top edges of the box indicate the 25th and 75th percentiles, respectively. If the groups are statistically different after post-hoc analysis, the significance levels are shown as: ***$p < .001$, **$p < .01$, and *$p < .05$.

S33, suggesting that depth weighting also improved the ability of wMEM to localize deep generators, while preserving good accuracy when localizing superficial generators, which could be of great interest when localizing specific oscillations using this wavelet extension of MEM framework.

4 | DISCUSSION

In this study, we proposed a depth-weighted implementation of cMEM for EEG/MEG source imaging to localize deep source activity accurately, while maintaining cMEM's ability to recover the spatial extent of the underlying generators for both deep and cortical generators. We assessed the ability of the depth-weighted method, $cMEM_{\omega}$ to localize simulated epileptic activity at different locations on the cortical and hippocampal surface. Compared to cMEM and MNE as benchmarks, the new version could estimate the deep generators more accurately, without or with minimal worsening of the localization for superficial regions. This was robust for HD-EEG and MEG, different spatial extents of the generator, and different SNR levels. A similar improvement was found for the wavelet version of the MEM method. We also demonstrated the utility of $cMEM_{\omega}$ in localizing

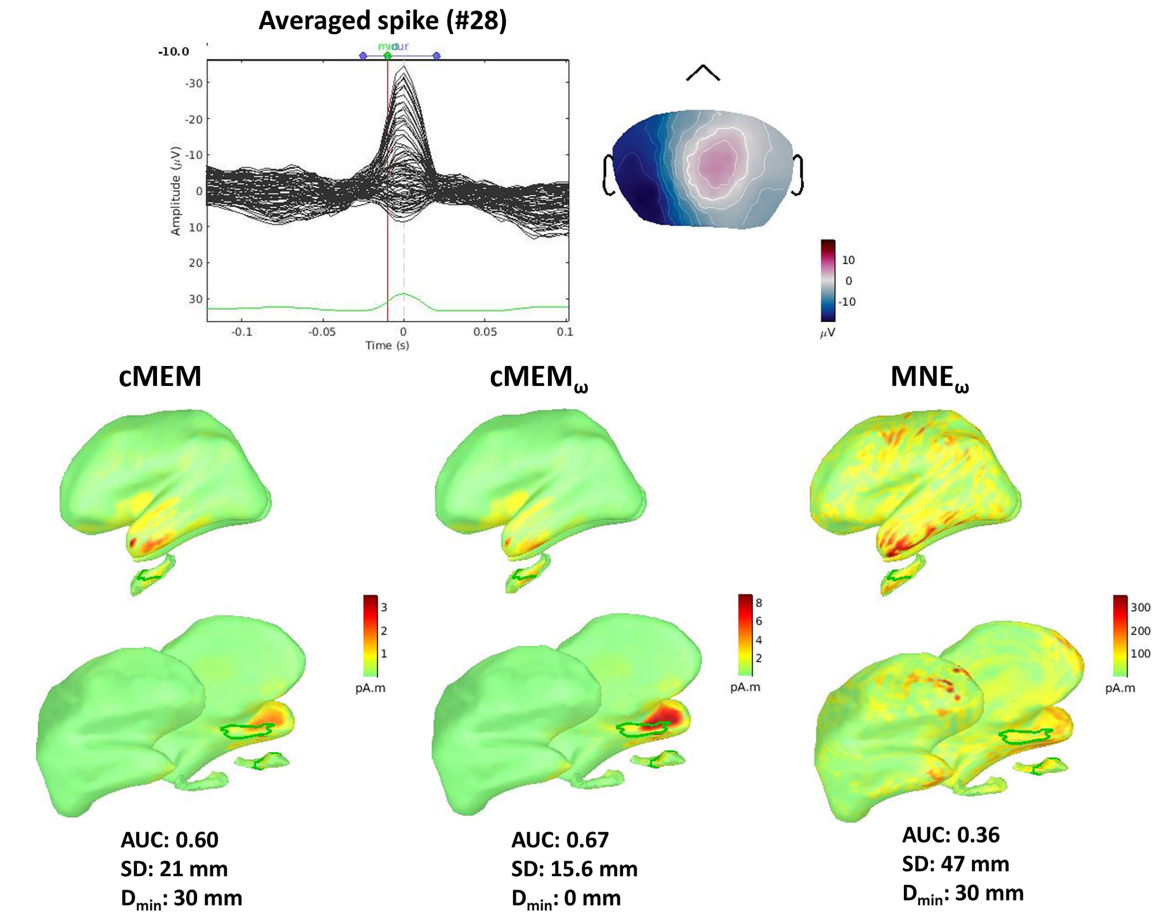

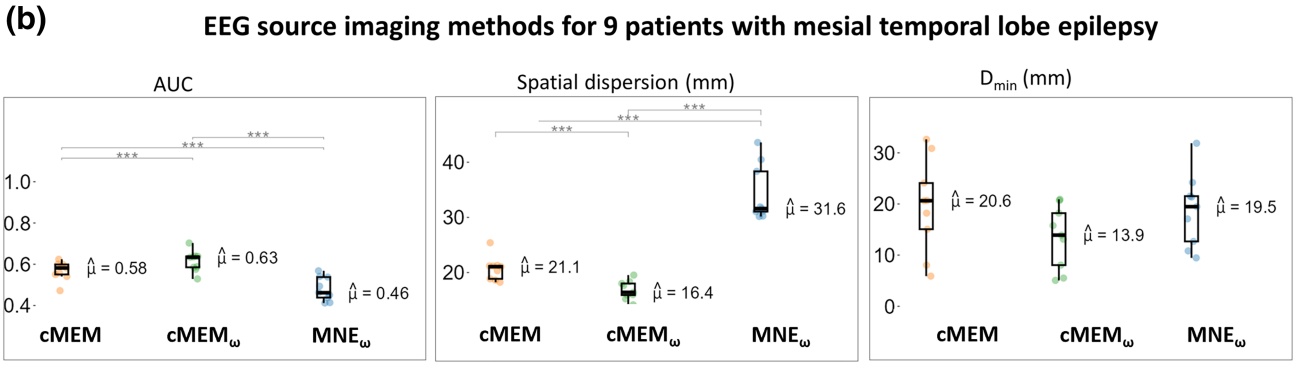

FIGURE 10 (a) Example localization of HD-EEG source imaging methods for a patient with mesial temporal lobe epilepsy. The source imaging methods were applied to an average of 28 interictal epileptic discharges. The surface of the hippocampus is included in the source model (shown as separate structures). The metrics AUC, SD, and D_{min} were calculated at the midpoint of the rising phase of the spike (−10 ms). The scale is different for the three methods but source maps are interpreted in a relative manner for each method. (b) Comparison of the EEG source imaging methods in terms of the validation metrics AUC, SD and D_{min} for nine patients with mesial temporal lobe epilepsy. Each boxplot represents metrics from one source imaging method. On each boxplot, the central mark indicates the median, and the bottom and top edges of the box indicate the 25th and 75th percentiles, respectively. If the groups are statistically different after posthoc analysis, the significance levels are shown as: ***p < .001, **p < .01, and *p < .05.

EEG/MEG epileptic spikes from patients with mesial temporal lobe epilepsy.

4.1 | Including hippocampus in the source model

The source model included the surface mesh of the cortex, with an additional subcortical structure, the hippocampus. The sources were located along the surface of the structures, with a fixed orientation normal to the surface as proposed by Attal and Schwartz (2013) and used in other studies (Calvetti et al., 2019; Meyer et al., 2017). Such modeling is motivated by the morphological and organizational similarity of the layer of the pyramidal cells in the hippocampus and neocortex (Meyer et al., 2017). Other subcortical structures such as the thalamus, amygdala, or brainstem can be modeled as a volume grid for better anatomical approximation (Attal & Schwartz, 2013). Including those structures in the volume grid would require handling parcellation in both surface and volume for the MEM framework, which was out of the scope of this study, as in MEM the parcellation is guided along the surface in a geodesic manner.

4.2 | Depth-weighted cMEM improved localization for deep sources

For MEG and HD-EEG simulations of epileptic activity involving different locations covering the whole brain, $cMEM_\omega$ provided more accurate localizations for deep sources than cMEM and MNE_ω. For superficial regions, $cMEM_\omega$ exhibited similar performance as cMEM in terms of AUC and D_{min}, but worsened slightly the SD. Compared to MNE_ω, $cMEM_\omega$ localizations for superficial regions were also better in terms of AUC and SD, along with our previous findings comparing non depth-weighted cMEM to MNE_ω (Chowdhury et al., 2013; Chowdhury et al., 2016; Chowdhury et al., 2018). Although $cMEM_\omega$ slightly worsened the SD compared to cMEM (by ~3 mm), it still provided improved SD compared to MNE_ω (by ~24 mm in MEG and ~ 14 mm for HD-EEG) and therefore excellent sensitivity to the spatial extent of the generators.

Our simulation results showed that the $cMEM_\omega$ was sensitive to mesial sources, and we found rare spurious localization of deep structures when they were not simulated. MEG and HD-EEG source imaging results were robust for all other combinations of spatial extent and SNR levels. Compared to HD-EEG, we observed high variance in SD and D_{min} for MEG simulations and worsening of SD and D_{min} for some superficial regions (Figures S5 and S22 and Figures 3 and 7). This was related to the lower level of sensor level SNR for MEG simulations compared to HD-EEG. The sensor level SNR of the simulated signal for MEG/HD-EEG is reflective of the sensitivity of the sensors to different source locations and orientations. For instance, EEG is more sensitive to radial and deep sources whereas MEG using gradiometers is more sensitive to tangential and superficial sources (Goldenholz et al., 2009; Kakisaka et al., 2013). This is also why the improvement in MEG due to depth weighting was more pronounced compared to HD-EEG (Figures 3 and 7). However, the low SNR of MEG simulations also resulted from the simulation model used in this study. As we used a uniform signal strength for all the vertices within a patch, the generators that consisted of two opposite walls of the sulcus would lead to more signal cancellation for MEG than EEG (Chowdhury et al., 2015; Chowdhury et al., 2016). Therefore, several MEG sources simulated in this study resulted in lower sensor level SNR when compared to HD-EEG. This could explain the large variance observed in SD and D_{min} in MEG localizations for both deep and superficial sources even after applying depth weighting.

Although $cMEM_\omega$ improved localization accuracy for deep sources compared to cMEM and MNE_ω, the localization accuracy was still associated with source depth (i.e., lower accuracy for deeper sources). This is consistent with the findings reported in previous studies using EEG (Krings et al., 1999; Mikulan et al., 2020; Unnwongse et al., 2023; Whittingstall et al., 2003) and MEG (Chowdhury et al., 2015). Using simultaneously acquired HD-EEG and intracerebral stimulation as ground truth, Pascarella et al. (2023) compared 10 source imaging methods and explored different depth weighting parameters. They found the lowest localization error (within 10 mm) was obtained for dipolar and sparsity-promoting localization methods. Larger localization errors (mean ~ 15–20 mm) were found for distributed source imaging methods such as the MNE_ω, sLORETA, eLORETA (Pascual-Marqui et al., 2006) and Beamformer (Van Veen et al., 1997), with large localization errors associated with deeper sources, even after applying depth weighting. In our HD-EEG simulations, we observed a similar range of localization error and SD for MNE_ω as reported by Pascarella et al. (2023). We found the lowest localization error (4.8 ± 6.8 mm) for $cMEM_\omega$. Both cMEM and $cMEM_\omega$ provided much lower SD compared to MNE_ω, consistent with our previous studies (Chowdhury et al., 2013; Chowdhury et al., 2016; Pellegrino, Hedrich, et al., 2020) reporting the ability of the MEM method to recover the spatial extent accurately. Pascarella et al. (2023) used real intracerebral stimulations resulting in very focal generators associated with high SNR, whereas we used realistic numerical simulations involving spatially extended generators and different SNR levels. Another important difference is we considered a fixed value of depth weighting factor ($\omega = 0.5$) for $cMEM_\omega$ and MNE_ω in the whole study. However, we also investigated the depth weighting parameter ω for a range of values: $\omega = 0.1, 0.3, 0.5, 0.7$, and 0.9 for one set of 300 MEG simulations (Figure S17). For deep sources, increasing the depth weighting parameter ω improved localization accuracy as expected, but choosing higher ω values penalized the localization of superficial sources. This observation aligns with Pascarella et al. (2023), who investigated different depth weightings between 0 and 5 in MNE, Mixed Norm Estimate (Gramfort et al., 2012), dSPM and Beamformer for various sources and found optimal localizations with either $\omega = 0$ or 1. This suggests that for superficial sources, $\omega = 0$ would provide the best localization, while for deep sources, $\omega = 1$ would be optimal. Without a ground truth, determining whether a source is superficial or deep is unknown. Therefore, choosing $\omega = 0.5$ appears as a reasonable compromise, whereas using 0 or 1 could potentially lead to complete mislocalization of sources. Moreover, the depth weighting factor

also depends on the sensitivity of the modality. For instance, Lin et al. (2006) reported the best localization accuracy for MNE_{ω} for a depth weighting factor ranging from 0.6 to 0.8 for MEG, and from 2 to 5 for EEG. Recently, in Cai et al. (2022), our group evaluated a range of ω when reconstructing functional Near-InfraRed Spectroscopy data using $cMEM_{\omega}$, most accurate results were found for depth weighting factors ranging between 0.3 and 0.5.

The simulations generated in this study were controlled to remain within a realistic range. Most of the hippocampal IEDs were nearly obscured by the background (as depicted in Figures S3 and S4). In contrast to single simulations in MEG, for the mixture of cortical and hippocampal sources, we intentionally applied a higher SNR for the hippocampus to highlight that even with a good SNR signal, the standard cMEM failed to localize accurately to the hippocampus. In scenarios with very low SNR, none of the methods would be able to effectively localize deep sources when they are obscured by the superficial component. However, this limitation would be due to the low SNR of deep sources rather than the methods themselves.

We also demonstrated the applicability of $cMEM_{\omega}$ by evaluating the source localization of actual IEDs from patients with focal epilepsy. For the patients with mesial temporal lobe epilepsy, localization was significantly improved by $cMEM_{\omega}$ compared to cMEM and MNE_{ω}. The MEG localizations of IEDs by cMEM were almost blind to the deep hippocampal or the mesial part of the sources. Depth weighting was necessary to localize these hippocampal sources during the rising phase of the spike. In contrast, HD-EEG localizations by cMEM were still behaving better (when compared to MEG) and some activity in the hippocampus and other deep regions was localized with cMEM, but incorporating depth weighting improved the localization accuracy.

4.3 | Complex simulations involving mesial and neocortical sources

It is evident from simultaneous recording of scalp EEG/MEG and intracerebral EEG that the IEDs generated in deep mesial structures are hardly observable (often missed during visual interpretation) from scalp measurements when confined to mesial structures only (Merlet & Gotman, 1999). The spikes generated from mesial structures are more detectable on the sensors when they propagate and involve the activation of neocortical sources (Koessler et al., 2015; Merlet & Gotman, 1999). To mimic such concurrent activation of mesial plus neocortical interictal spikes, we simulated complex epileptic spikes on MEG, including the first generator at the hippocampus propagating to a second generator on the temporal neocortex after 15 ms. We only ran these simulations for MEG, not HD-EEG, because it was more difficult for MEG data acquired with gradiometers to localize deep sources without depth weighting, when compared to our HD-EEG results. We considered source imaging at the peak of the hippocampal sources, which corresponded approximately to the midpoint of the rising phase of the spike we used when localizing clinical data. Compared to cMEM and MNE_{ω}, $cMEM_{\omega}$ was more accurate when localizing the hippocampal source. cMEM could not localize the hippocampal source, mistakenly placing it on the lateral neocortex. $cMEM_{\omega}$ localized the source in the hippocampus, but also exhibited spurious localizations on the lateral neocortex, reflected by a large localization error (∼20 mm) and SD (∼25 mm). MNE_{ω} also showed this spurious localization on the lateral neocortex reflected by large localization error (∼28 mm) and spatial spread (SD: ∼48 mm). For superficial regions, localizations by both MEM methods were more accurate than MNE_{ω} in terms of AUC and SD, not in terms of D_{min}, as we previously reported (Hedrich et al., 2017).

Although $cMEM_{\omega}$ was more accurate than cMEM in localizing the deep hippocampal activity, the maximum activity was mostly found on the lateral cortex (see D_{min} in Figure 6). This activation in the lateral cortex was also contributed by the simulation of the neocortical generator that already started at that point. However, we also observed spurious activity on the lateral neocortex for the single sources simulated in the hippocampus only, which was reflected by high SD. Thus, the challenge to completely disentangle the mesial from neocortical sources remains (Benar et al., 2021; Krishnaswamy et al., 2017), even if depth weighting shows improved accuracy in localizing deep generators. Independent component analysis (ICA) based source separation techniques could be employed to disentangle deep versus superficial sources (Pizzo et al., 2019). However, ICA-based approach has been found to worsen MEG source localization accuracy for interictal activity and is suggested to be applied with caution (Pellegrino, Xu, et al., 2020).

4.4 | Sensitivity of EEG/MEG sensors to deep activity

As the simulations for MEG and HD-EEG were implemented using background activity and anatomical head models from two different subjects, it was difficult to compare different source localization methods between these modalities directly. However, MEG was found overall less sensitive to deep sources than HD-EEG. One of the main reasons is that we considered gradiometers only, whereas magnetometers have a higher sensitivity to deep sources, at the price of more sensitivity to environmental noise (Malmivuo & Plonsey, 1995; Parkkonen et al., 2009). Our results are therefore consistent with studies using MEG gradiometers and suggesting that MEG is less sensitive to deep sources (Agirre-Arrizubieta et al., 2009; Baumgartner et al., 2000; Leijten et al., 2003; Shigeto et al., 2002; Wennberg et al., 2011). Few studies localizing subcortical activity using gradiometers benefitted from evoked responses with large SNR data (Barry et al., 2019; Coffey et al., 2016; Taylor et al., 2011). In contrast, most studies reporting that deep activity is indeed detectable by MEG, used magnetometers (Dalal et al., 2013; López-Madrona et al., 2022; Pizzo et al., 2019; Plummer et al., 2019; Santiuste et al., 2008). Fusion of EEG and MEG can also be exploited to recover some deep activity which we previously demonstrated using cMEM (Chowdhury et al., 2015; Chowdhury et al., 2018). Even though gradiometers are less sensitive to deep sources, we showed that the proposed $cMEM_{\omega}$ method would be useful for localizing deep source activity, even for gradiometers.

4.5 | Depth-weighted wMEM

wMEM represents the data on the time-frequency domain, using discrete wavelets, before applying MEM solver for localization. Since discrete wavelets only consider the oscillatory part of the signal, wMEM was therefore proposed as a method particularly adapted to localize brain oscillations (Lina et al., 2012). The depth-weighted wMEM (wMEMω), the wavelet version of $cMEM_\omega$, showed similar improvement for MEG and HD-EEG simulations. Compared to $cMEM_\omega$, $wMEM_\omega$ results exhibited similar performances in terms of AUC and D_{min}, but slightly larger SD values. We expect that wMEM localization of epileptic spikes, mainly characterized by a transient shape and not by oscillations, will often result in higher SD than cMEM. The depth-weighted version of wMEM is more suitable for the localization of resting state oscillations (Afnan et al., 2023), epileptic burst activity, or high-frequency oscillations from deep sources (Avigdor et al., 2021; von Ellenrieder et al., 2016) and oscillatory activity at seizure onset (Pellegrino et al., 2016).

4.6 | Limitations

One limitation of this study is that the MEG and EEG simulations were generated using anatomical head models and background recordings from different subjects, thus it was difficult to directly compare these two modalities. Simultaneous recording of EEG and MEG on the same subject would allow a comparison of the sensitivity of detecting deep source activity by EEG versus MEG. Moreover, the ground truth used for patients was still semi-quantitative. Further examination showed that the differences in localization improvement by depth weighting between the seizure-free group and the other group were not likely influenced by the quality of ground truth and possibly by the number of patients with deep generators included in that group (see Data S2, Tables S1 and S2). Comparison of simultaneous scalp recording with intracranial EEG will be considered in our future investigations.

5 | CONCLUSION

We proposed depth-weighted cMEM ($cMEM_\omega$) source imaging and demonstrated that it improved the EEG/MEG localization of deep sources compared to standard cMEM and depth-weighted MNE. We validated this method using extensive MEG and EEG realistic simulations of epileptic spikes, covering all brain regions including the hippocampus. We demonstrated the improvement by $cMEM_\omega$ in localizing deep brain activity, especially in a low SNR environment. Finally, we showed that $cMEM_\omega$ could localize the hippocampal activity more accurately for patients with mesial temporal lobe epilepsy, in cases for which standard cMEM would fail in recovering these deep generators. It is notable that the localization of superficial sources was hardly affected by depth weighting both for MEG and HD-EEG.

ACKNOWLEDGMENTS

This study was supported by Natural Sciences and Engineering Research Council of Canada (NSERC) Discovery grant, grant from Canadian Institutes of Health Research (CIHR) (PJT-159948 and FDN 143208), and the Fonds de recherche du Québec—Nature et technologies (FRQNT) Research team grant. JA was partially supported by The Canadian Open Neuroscience Platform scholarship, Irma Bauer Fellowship, Faculty of Medicine and Health Sciences, McGill University and Fonds de Recherche du Québec—Santé Doctoral scholarship. BF was supported by CIHR project grant (PJT-175056), salary award (Chercheur-boursier clinicien Senior) of the Fonds de Recherche du Québec—Santé.

CONFLICT OF INTEREST STATEMENT

The authors declare no conflict of interest.

DATA AVAILABILITY STATEMENT

The data that support the findings of this study are available on request from the corresponding author. The data are not publicly available due to privacy or ethical restrictions.

ORCID

Jawata Afnan https://orcid.org/0000-0003-3206-9873
Zhengchen Cai https://orcid.org/0000-0002-4233-5568
Edouard Delaire https://orcid.org/0000-0003-1421-1071
Tanguy Hedrich https://orcid.org/0000-0002-6238-5415
Nicolas von Ellenrieder https://orcid.org/0000-0003-0845-347X
Birgit Frauscher https://orcid.org/0000-0001-6064-1529
Christophe Grova https://orcid.org/0000-0003-2775-9968

REFERENCES

Abdallah, C., Hedrich, T., Koupparis, A., Afnan, J., Hall, J. A., Gotman, J., Dubeau, F., von Ellenrieder, N., Frauscher, B., Kobayashi, E., & Grova, C. (2022). Clinical yield of electromagnetic source imaging and hemodynamic responses in epilepsy: Validation with intracerebral data. *Neurology*, *98*(24), e2499–e2511.

Afnan, J., von Ellenrieder, N., Lina, J.-M., Pellegrino, G., Arcara, G., Cai, Z., Hedrich, T., Abdallah, C., Khajehpour, H., Frauscher, B., Gotman, J., & Grova, C. (2023). Validating MEG source imaging of resting state oscillatory patterns with an intracranial EEG atlas. *NeuroImage*, *274*, 120158.

Agirre-Arrizubieta, Z., Huiskamp, G., Ferrier, C., Van Huffelen, A., & Leijten, F. (2009). Interictal magnetoencephalography and the irritative zone in the electrocorticogram. *Brain*, *132*(11), 3060–3071.

Alberto, G. E., Stapleton-Kotloski, J. R., Klorig, D. C., Rogers, E. R., Constantinidis, C., Daunais, J. B., & Godwin, D. W. (2021). MEG source imaging detects optogenetically-induced activity in cortical and subcortical networks. *Nature Communications*, *12*(1), 5259.

Amblard, C., Lapalme, E., & Lina, J.-M. (2004). Biomagnetic source detection by maximum entropy and graphical models. *IEEE Transactions on Biomedical Engineering*, *51*(3), 427–442.

Attal, Y., Bhattacharjee, M., Yelnik, J., Cottereau, B., Lefèvre, J., Okada, Y., Bardinet, E., Chupin, M., & Baillet, S. (2009). Modelling and detecting deep brain activity with MEG and EEG. *IRBM*, *30*, 133–138.

Attal, Y., & Schwartz, D. (2013). Assessment of subcortical source localization using deep brain activity imaging model with minimum norm operators: A MEG study. *PLoS One*, *8*(3), e59856.

Avigdor, T., Abdallah, C., Afnan, J., Cai, Z., Rammal, S., Grova, C., & Frauscher, B. (2024). Consistency of electrical source imaging in presurgical evaluation of epilepsy across different vigilance states. *Annals of Clinical and Translational Neurology*, *11*(2), 389–403.

Avigdor, T., Abdallah, C., von Ellenrieder, N., Hedrich, T., Rubino, A., Russo, G. L., Bernhardt, B., Nobili, L., Grova, C., & Frauscher, B. (2021). Fast oscillations >40 Hz localize the epileptogenic zone: An electrical source imaging study using high-density electroencephalography. *Clinical Neurophysiology*, *132*(2), 568–580.

Barkley, G. L., & Baumgartner, C. (2003). MEG and EEG in epilepsy. *Journal of Clinical Neurophysiology*, *20*(3), 163–178.

Barry, D. N., Barnes, G. R., Clark, I. A., & Maguire, E. A. (2019). The neural dynamics of novel scene imagery. *Journal of Neuroscience*, *39*(22), 4375–4386.

Baumgartner, C., Pataraia, E., Lindinger, G., & Deecke, L. (2000). Neuromagnetic recordings in temporal lobe epilepsy. *Journal of Clinical Neurophysiology*, *17*(2), 177–189.

Bautista, R. E. D., Cobbs, M. A., Spencer, D. D., & Spencer, S. S. (1999). Prediction of surgical outcome by interictal epileptiform abnormalities during intracranial EEG monitoring in patients with extrahippocampal seizures. *Epilepsia*, *40*(7), 880–890.

Benar, C.-G., Velmurugan, J., Lopez-Madrona, V. J., Pizzo, F., & Badier, J.-M. (2021). Detection and localization of deep sources in magnetoencephalography: A review. *Current Opinion in Biomedical Engineering*, *18*, 100285.

Cai, Z., Machado, A., Chowdhury, R. A., Spilkin, A., Vincent, T., Aydin, Ü., Pellegrino, G., Lina, J.-M., & Grova, C. (2022). Diffuse optical reconstructions of functional near infrared spectroscopy data using maximum entropy on the mean. *Scientific Reports*, *12*(1), 1–18.

Calvetti, D., Pascarella, A., Pitolli, F., Somersalo, E., & Vantaggi, B. (2019). Brain activity mapping from MEG data via a hierarchical Bayesian algorithm with automatic depth weighting. *Brain Topography*, *32*, 363–393.

Chowdhury, R., Merlet, I., Birot, G., Kobayashi, E., Nica, A., Biraben, A., Wendling, F., Lina, J.-M., Albera, L., & Grova, C. (2016). Complex patterns of spatially extended generators of epileptic activity: Comparison of source localization methods cMEM and 4-ExSo-MUSIC on high resolution EEG and MEG data. *NeuroImage*, *143*, 175–195.

Chowdhury, R. A., Lina, J. M., Kobayashi, E., & Grova, C. (2013). MEG source localization of spatially extended generators of epileptic activity: Comparing entropic and hierarchical bayesian approaches. *PLoS One*, *8*(2), e55969.

Chowdhury, R. A., Pellegrino, G., Aydin, Ü., Lina, J. M., Dubeau, F., Kobayashi, E., & Grova, C. (2018). Reproducibility of EEG-MEG fusion source analysis of interictal spikes: Relevance in presurgical evaluation of epilepsy. *Human Brain Mapping*, *39*(2), 880–901.

Chowdhury, R. A., Zerouali, Y., Hedrich, T., Heers, M., Kobayashi, E., Lina, J.-M., & Grova, C. (2015). MEG–EEG information fusion and electromagnetic source imaging: From theory to clinical application in epilepsy. *Brain Topography*, *28*, 785–812.

Coffey, E. B., Herholz, S. C., Chepesiuk, A. M., Baillet, S., & Zatorre, R. J. (2016). Cortical contributions to the auditory frequency-following response revealed by MEG. *Nature Communications*, *7*(1), 11070.

Dalal, S., Jerbi, K., Bertrand, O., Adam, C., Ducorps, A., Schwartz, D., Martinerie, J., & Lachaux, J.-P. (2013). Simultaneous MEG-intracranial EEG: New insights into the ability of MEG to capture oscillatory modulations in the neocortex and the hippocampus. *Epilepsy & Behavior*. https://doi.org/10.1016/j.yebeh.2013.1003.1012

Dalal, S. S., Baillet, S., Adam, C., Ducorps, A., Schwartz, D., Jerbi, K., Bertrand, O., Garnero, L., Martinerie, J., & Lachaux, J.-P. (2009). Simultaneous MEG and intracranial EEG recordings during attentive reading. *NeuroImage*, *45*(4), 1289–1304.

Dale, A. M., Fischl, B., & Sereno, M. I. (1999). Cortical surface-based analysis: I. Segmentation and surface reconstruction. *NeuroImage*, *9*(2), 179–194.

Dale, A. M., Liu, A. K., Fischl, B. R., Buckner, R. L., Belliveau, J. W., Lewine, J. D., & Halgren, E. (2000). Dynamic statistical parametric mapping: Combining fMRI and MEG for high-resolution imaging of cortical activity. *Neuron*, *26*(1), 55–67.

Ebersole, J. S. (1997). Defining epileptogenic foci: past, present, future. *Journal of Clinical Neurophysiology*, *14*(6), 470–483.

Friston, K., Harrison, L., Daunizeau, J., Kiebel, S., Phillips, C., Trujillo-Barreto, N., Henson, R., Flandin, G., & Mattout, J. (2008). Multiple sparse priors for the M/EEG inverse problem. *NeuroImage*, *39*(3), 1104–1120.

Fuchs, M., Wagner, M., Köhler, T., & Wischmann, H.-A. (1999). Linear and nonlinear current density reconstructions. *Journal of Clinical Neurophysiology*, *16*(3), 267–295.

Goldenholz, D. M., Ahlfors, S. P., Hämäläinen, M. S., Sharon, D., Ishitobi, M., Vaina, L. M., & Stufflebeam, S. M. (2009). Mapping the signal-to-noise-ratios of cortical sources in magnetoencephalography and electroencephalography. *Human Brain Mapping*, *30*(4), 1077–1086.

Gramfort, A., Kowalski, M., & Hämäläinen, M. (2012). Mixed-norm estimates for the M/EEG inverse problem using accelerated gradient methods. *Physics in Medicine & Biology*, *57*(7), 1937–1961.

Grova, C., Aiguabella, M., Zelmann, R., Lina, J. M., Hall, J. A., & Kobayashi, E. (2016). Intracranial EEG potentials estimated from MEG sources: A new approach to correlate MEG and iEEG data in epilepsy. *Human Brain Mapping*, *37*(5), 1661–1683.

Grova, C., Daunizeau, J., Lina, J.-M., Bénar, C. G., Benali, H., & Gotman, J. (2006). Evaluation of EEG localization methods using realistic simulations of interictal spikes. *NeuroImage*, *29*(3), 734–753.

Hämäläinen, M. S., & Ilmoniemi, R. J. (1994). Interpreting magnetic fields of the brain: Minimum norm estimates. *Medical & Biological Engineering & Computing*, *32*, 35–42.

Hari, R. (1990). The neuromagnetic method in the study of the human auditory cortex. In *Auditory Evoked Magnetic Fields and Potentials: Advances in Audiology* (Vol. 6, pp. 222–282). Karger.

Hauf, M., Jann, K., Schindler, K., Scheidegger, O., Meyer, K., Rummel, C., Mariani, L., König, T., & Wiest, R. (2012). Localizing seizure-onset zones in presurgical evaluation of drug-resistant epilepsy by electroencephalography/fMRI: Effectiveness of alternative thresholding strategies. *American Journal of Neuroradiology*, *33*(9), 1818–1824.

Hedrich, T., Pellegrino, G., Kobayashi, E., Lina, J.-M., & Grova, C. (2017). Comparison of the spatial resolution of source imaging techniques in high-density EEG and MEG. *NeuroImage*, *157*, 531–544.

Heller, L., & van Hulsteyn, D. B. (1992). Brain stimulation using electromagnetic sources: Theoretical aspects. *Biophysical Journal*, *63*(1), 129–138.

Hufnagel, A., Dümpelmann, M., Zentner, J., Schijns, O., & Elger, C. (2000). Clinical relevance of quantified intracranial interictal spike activity in presurgical evaluation of epilepsy. *Epilepsia*, *41*(4), 467–478.

Jeffs, B., Leahy, R., & Singh, M. (1987). An evaluation of methods for neuromagnetic image reconstruction. *IEEE Transactions on Biomedical Engineering*, *9*, 713–723.

Kaiboriboon, K., Nagarajan, S., Mantle, M., & Kirsch, H. E. (2010). Interictal MEG/MSI in intractable mesial temporal lobe epilepsy: Spike yield and characterization. *Clinical Neurophysiology*, *121*(3), 325–331.

Kakisaka, Y., Alkawadri, R., Wang, Z. I., Enatsu, R., Mosher, J. C., Dubarry, A.-S., Alexopoulos, A. V., & Burgess, R. C. (2013). Sensitivity of scalp 10–20 EEG and magnetoencephalography. *Epileptic Disorders*, *15*, 27–31.

Koessler, L., Cecchin, T., Colnat-Coulbois, S., Vignal, J.-P., Jonas, J., Vespignani, H., Ramantani, G., & Maillard, L. G. (2015). Catching the invisible: Mesial temporal source contribution to simultaneous EEG and SEEG recordings. *Brain Topography*, *28*, 5–20.

Krings, T., Chiappa, K. H., Cuffin, B. N., Cochius, J. I., Connolly, S., & Cosgrove, G. R. (1999). Accuracy of EEG dipole source localization using implanted sources in the human brain. *Clinical Neurophysiology*, *110*(1), 106–114.

Krishnaswamy, P., Obregon-Henao, G., Ahveninen, J., Khan, S., Babadi, B., Iglesias, J. E., Hämäläinen, M. S., & Purdon, P. L. (2017). Sparsity

enables estimation of both subcortical and cortical activity from MEG and EEG. *Proceedings of the National Academy of Sciences*, *114*(48), E10465–E10474.

Kybic, J., Clerc, M., Abboud, T., Faugeras, O., Keriven, R., & Papadopoulo, T. (2005). A common formalism for the integral formulations of the forward EEG problem. *IEEE Transactions on Medical Imaging*, *24*(1), 12–28.

Lapalme, E., Lina, J.-M., & Mattout, J. (2006). Data-driven parceling and entropic inference in MEG. *NeuroImage*, *30*(1), 160–171.

Leijten, F. S., Huiskamp, G.-J. M., Hilgersom, I., & Van Huffelen, A. C. (2003). High-resolution source imaging in mesiotemporal lobe epilepsy: A comparison between MEG and simultaneous EEG. *Journal of Clinical Neurophysiology*, *20*(4), 227–238.

Lin, F.-H., Witzel, T., Ahlfors, S. P., Stufflebeam, S. M., Belliveau, J. W., & Hämäläinen, M. S. (2006). Assessing and improving the spatial accuracy in MEG source localization by depth-weighted minimum-norm estimates. *NeuroImage*, *31*(1), 160–171.

Lina, J.-M., Chowdhury, R., Lemay, E., Kobayashi, E., & Grova, C. (2012). Wavelet-based localization of oscillatory sources from magnetoencephalography data. *IEEE Transactions on Biomedical Engineering*, *61*(8), 2350–2364.

López-Madrona, V. J., Medina Villalon, S., Badier, J. M., Trébuchon, A., Jayabal, V., Bartolomei, F., Carron, R., Barborica, A., Vulliémoz, S., Alario, F. X., & Bénar, C. G. (2022). Magnetoencephalography can reveal deep brain network activities linked to memory processes. *Human Brain Mapping*, *43*(15), 4733–4749.

Lorente De Nó, R. (1947). Action potential of the motoneurons of the hypoglossus nucleus. *Journal of Cellular and Comparative Physiology*, *29*(3), 207–287.

Malmivuo, J., & Plonsey, R. (1995). *Bioelectromagnetism: Principles and applications of bioelectric and biomagnetic fields*. Oxford University Press.

Merlet, I., & Gotman, J. (1999). Reliability of dipole models of epileptic spikes. *Clinical Neurophysiology*, *110*(6), 1013–1028.

Meyer, S. S., Rossiter, H., Brookes, M. J., Woolrich, M. W., Bestmann, S., & Barnes, G. R. (2017). Using generative models to make probabilistic statements about hippocampal engagement in MEG. *NeuroImage*, *149*, 468–482.

Mikulan, E., Russo, S., Parmigiani, S., Sarasso, S., Zauli, F. M., Rubino, A., Avanzini, P., Cattani, A., Sorrentino, A., Gibbs, S., Cardinale, F., Sartori, I., Nobili, L., Massimini, M., & Pigorini, A. (2020). Simultaneous human intracerebral stimulation and HD-EEG, ground-truth for source localization methods. *Scientific Data*, *7*(1), 127.

Mikuni, N., Nagamine, T., Ikeda, A., Terada, K., Taki, W., Kimura, J., Kikuchi, H., & Shibasaki, H. (1997). Simultaneous recording of epileptiform discharges by MEG and subdural electrodes in temporal lobe epilepsy. *NeuroImage*, *5*(4), 298–306.

Murakami, S., & Okada, Y. (2006). Contributions of principal neocortical neurons to magnetoencephalography and electroencephalography signals. *The Journal of Physiology*, *575*(3), 925–936.

Oishi, M., Otsubo, H., Kameyama, S., Morota, N., Masuda, H., Kitayama, M., & Tanaka, R. (2002). Epileptic spikes: Magnetoencephalography versus simultaneous electrocorticography. *Epilepsia*, *43*(11), 1390–1395.

Parkkonen, L., Fujiki, N., & Mäkelä, J. P. (2009). Sources of auditory brainstem responses revisited: Contribution by magnetoencephalography. *Human Brain Mapping*, *30*(6), 1772–1782.

Pascarella, A., Mikulan, E., Sciacchitano, F., Sarasso, S., Rubino, A., Sartori, I., Cardinale, F., Zauli, F., Avanzini, P., Nobili, L., Pigorini, A., & Sorrentino, A. (2023). An in-vivo validation of ESI methods with focal sources. *NeuroImage*, *277*, 120219.

Pascual-Marqui, R. D. (2002). Standardized low-resolution brain electromagnetic tomography (sLORETA): Technical details. *Methods and Findings in Experimental and Clinical Pharmacology*, *24*(Suppl D), 5–12.

Pascual-Marqui, R. D., Pascual-Montano, A. D., Lehmann, D., Kochi, K., Esslen, M., Jancke, L., Anderer, P., Saletu, B., Tanaka, H., Hirata, K., & John, E. R. (2006). Exact low resolution brain electromagnetic tomography (eLORETA). *NeuroImage*, *31*(Suppl 1), S86.

Pellegrino, G., Hedrich, T., Chowdhury, R., Hall, J. A., Lina, J. M., Dubeau, F., Kobayashi, E., & Grova, C. (2016). Source localization of the seizure onset zone from ictal EEG/MEG data. *Human Brain Mapping*, *37*(7), 2528–2546.

Pellegrino, G., Hedrich, T., Chowdhury, R. A., Hall, J. A., Dubeau, F., Lina, J. M., Kobayashi, E., & Grova, C. (2018). Clinical yield of magnetoencephalography distributed source imaging in epilepsy: A comparison with equivalent current dipole method. *Human Brain Mapping*, *39*(1), 218–231.

Pellegrino, G., Hedrich, T., Porras-Bettancourt, M., Lina, J. M., Aydin, Ü., Hall, J., Grova, C., & Kobayashi, E. (2020). Accuracy and spatial properties of distributed magnetic source imaging techniques in the investigation of focal epilepsy patients. *Human Brain Mapping*, *41*(11), 3019–3033.

Pellegrino, G., Xu, M., Alkuwaiti, A., Porras-Bettancourt, M., Abbas, G., Lina, J.-M., Grova, C., & Kobayashi, E. (2020). Effects of independent component analysis on magnetoencephalography source localization in pre-surgical frontal lobe epilepsy patients. *Frontiers in Neurology*, *11*, 479.

Pizzo, F., Roehri, N., Medina Villalon, S., Trébuchon, A., Chen, S., Lagarde, S., Carron, R., Gavaret, M., Giusiano, B., McGonigal, A., Bartolomei, F., Badier, J. M., & Bénar, C. G. (2019). Deep brain activities can be detected with magnetoencephalography. *Nature Communications*, *10*(1), 1–13.

Plummer, C., Vogrin, S. J., Woods, W. P., Murphy, M. A., Cook, M. J., & Liley, D. T. (2019). Interictal and ictal source localization for epilepsy surgery using high-density EEG with MEG: A prospective long-term study. *Brain*, *142*(4), 932–951.

Rampp, S., & Stefan, H. (2007). Magnetoencephalography in presurgical epilepsy diagnosis. *Expert Review of Medical Devices*, *4*(3), 335–347.

Rosenow, F., & Lüders, H. (2001). Presurgical evaluation of epilepsy. *Brain*, *124*(9), 1683–1700.

Santiuste, M., Nowak, R., Russi, A., Tarancon, T., Oliver, B., Ayats, E., Scheler, G., & Graetz, G. (2008). Simultaneous magnetoencephalography and intracranial EEG registration: Technical and clinical aspects. *Journal of Clinical Neurophysiology*, *25*(6), 331–339.

Seeber, M., Cantonas, L.-M., Hoevels, M., Sesia, T., Visser-Vandewalle, V., & Michel, C. M. (2019). Subcortical electrophysiological activity is detectable with high-density EEG source imaging. *Nature Communications*, *10*(1), 753.

Shigeto, H., Morioka, T., Hisada, K., Nishio, S., Ishibashi, H., Kira, D.-I., Tobimatsu, S., & Kato, M. (2002). Feasibility and limitations of magnetoencephalographic detection of epileptic discharges: Simultaneous recording of magnetic fields and electrocorticography. *Neurological Research*, *24*(6), 531–536.

Tadel, F., Baillet, S., Mosher, J. C., Pantazis, D., & Leahy, R. M. (2011). Brainstorm: A user-friendly application for MEG/EEG analysis. *Computational Intelligence and Neuroscience*, *2011*, 1–13.

Tadel, F., Bock, E., Niso, G., Mosher, J. C., Cousineau, M., Pantazis, D., Leahy, R. M., & Baillet, S. (2019). MEG/EEG group analysis with brainstorm. *Frontiers in Neuroscience*, *13*, 435877.

Tao, J. X., Baldwin, M., Hawes-Ebersole, S., & Ebersole, J. S. (2007). Cortical substrates of scalp EEG epileptiform discharges. *Journal of Clinical Neurophysiology*, *24*(2), 96–100.

Taylor, M. J., Mills, T., & Pang, E. W. (2011). The development of face recognition; hippocampal and frontal lobe contributions determined with MEG. *Brain Topography*, *24*, 261–270.

Unnwongse, K., Rampp, S., Wehner, T., Kowoll, A., Parpaley, Y., von Lehe, M., Lanfer, B., Rusiniak, M., Wolters, C., & Wellmer, J. (2023). Validating EEG source imaging using intracranial electrical stimulation. *Brain Communications*, *5*(1), fcad023.

Uusitalo, M. A., & Ilmoniemi, R. J. (1997). Signal-space projection method for separating MEG or EEG into components. *Medical and Biological Engineering and Computing*, *35*(2), 135–140.

Uutela, K., Hämäläinen, M., & Somersalo, E. (1999). Visualization of magnetoencephalographic data using minimum current estimates. *NeuroImage*, *10*(2), 173–180.

van Veen, B. D., van Drongelen, W., Yuchtman, M., & Suzuki, A. (1997). Localization of brain electrical activity via linearly constrained minimum variance spatial filtering. *IEEE Transactions on Biomedical Engineering*, *44*(9), 867–880.

von Ellenrieder, N., Beltrachini, L., Muravchik, C. H., & Gotman, J. (2014). Extent of cortical generators visible on the scalp: Effect of a subdural grid. *NeuroImage*, *101*, 787–795.

von Ellenrieder, N., Pellegrino, G., Hedrich, T., Gotman, J., Lina, J.-M., Grova, C., & Kobayashi, E. (2016). Detection and magnetic source imaging of fast oscillations (40–160 Hz) recorded with magnetoencephalography in focal epilepsy patients. *Brain Topography*, *29*(2), 218–231.

Wennberg, R., Valiante, T., & Cheyne, D. (2011). EEG and MEG in mesial temporal lobe epilepsy: Where do the spikes really come from? *Clinical Neurophysiology*, *122*(7), 1295–1313.

Whittingstall, K., Stroink, G., Gates, L., Connolly, J., & Finley, A. (2003). Effects of dipole position, orientation and noise on the accuracy of EEG source localization. *Biomedical Engineering Online*, *2*(1), 1–5.

Zhang, Y., van Drongelen, W., & He, B. (2006). Estimation of in vivo brain-to-skull conductivity ratio in humans. *Applied Physics Letters*, *89*(22), 223903.

SUPPORTING INFORMATION

Additional supporting information can be found online in the Supporting Information section at the end of this article.

How to cite this article: Afnan, J., Cai, Z., Lina, J.-M., Abdallah, C., Delaire, E., Avigdor, T., Ros, V., Hedrich, T., von Ellenrieder, N., Kobayashi, E., Frauscher, B., Gotman, J., & Grova, C. (2024). EEG/MEG source imaging of deep brain activity within the maximum entropy on the mean framework: Simulations and validation in epilepsy. *Human Brain Mapping*, *45*(10), e26720. https://doi.org/10.1002/hbm.26720

APPENDIX A

A.1 | Coherent maximum entropy on the mean (cMEM)

The relationship between source amplitudes and EEG/MEG measurements is expressed by the following linear model:

$$\boldsymbol{m}(t) = \mathbf{G}\mathbf{j}(t) + \boldsymbol{e}(t) \tag{A1}$$

$\boldsymbol{m}(t)$ is the q-dimensional measurement vector for EEG or MEG signal at time t where q denotes the number of EEG/MEG sensors, $\mathbf{j}(t)$ is the r-dimensional vector denoting current density of r dipolar sources at time t and $\mathbf{G}$ is the lead field matrix with a dimension of $q \times r$. $\boldsymbol{e}(t)$ models an additive measurement noise at time t. We assume an anatomical constraint that the dipoles are orientated orthogonally to the surface of the cortex and hippocampus.

Within the MEM framework (Amblard et al., 2004), $\mathbf{j}$ denoting the intensities of r dipolar sources is considered as a random variable described by the probability distribution $dp(\mathbf{j}) = p(\mathbf{j})d\mathbf{j}$. To regularize the inverse problem, we incorporate prior information on $\mathbf{j}$ in the form of a reference distribution $d\nu(\mathbf{j})$. The Kullback Leibler divergence or ν-entropy is defined by:

$$S_\nu(dp) = -\int_{\mathbf{j}} \log\left(\frac{dp(\mathbf{j})}{d\nu(\mathbf{j})}\right) dp(\mathbf{j}) = -\int_{\mathbf{j}} f(\mathbf{j}) \log(f(\mathbf{j})) d\nu(\mathbf{j}) \tag{A2}$$

where f is a ν-density of dp defined as $dp(\mathbf{j}) = f(\mathbf{j})d\nu(\mathbf{j})$. The ν-entropy $S_\nu(dp)$ measures the amount of information brought by the data with respect to the prior $d\nu$. We introduce a data fit constraint as the set of probability distributions on $\mathbf{j}$ that explains the data on average.

$$\boldsymbol{m} - [\boldsymbol{G}|\boldsymbol{I}_q]\begin{bmatrix} \mathrm{E}_{dp}[\mathbf{j}] \\ \boldsymbol{e} \end{bmatrix} = 0, dp \in C_M \tag{A3}$$

where C_M is the set of probability distributions on $\mathbf{j}$ that explains the data on average, $\mathrm{E}_{dp}[\mathbf{j}] = \int_{j\in\Omega} \mathbf{j}\, dp(\mathbf{j})$ is the mathematical expectation of $\mathbf{j}$ with respect to the probability distribution dp and $\boldsymbol{I}_q$ is a $q \times q$ identity matrix. Among all the possible distributions of $dp(\mathbf{j})$ that explain the data $\boldsymbol{m}$ on average, MEM solution is derived from maximizing the ν-entropy (Amblard et al., 2004; Grova et al., 2006). More details on MEM formulations are described in Chowdhury et al. (2016). The key feature of this framework is a spatial prior model, assuming that brain activity is organized within a set of K non-overlapping and independent parcels. The reference distribution $d\nu(\mathbf{j})$ for K parcels is defined as a joint distribution:

$$d\nu(\mathbf{j}) = d\nu_1(\mathbf{j}_1)d\nu_2(\mathbf{j}_2)d\nu_3(\mathbf{j}_3).....d\nu_k(\mathbf{j}_k).....d\nu_K(\mathbf{j}_K) \tag{A4}$$

The spatial parcellation used in MEM method uses a data driven parcellation technique (Lapalme et al., 2006). Each parcel k is characterized by an activation state S_k, which is a hidden state variable controlling the activation of the parcel. The reference distribution for each parcel is defined as:

$$d\nu_k(\mathbf{j}_k) = [(1-\alpha_k)\delta(\mathbf{j}_k) + \alpha_k \mathcal{N}(\boldsymbol{\mu}_k, \boldsymbol{\Sigma}_k)(\mathbf{j}_k)]d\mathbf{j}_k \tag{A5}$$

where α_k is the probability of the kth parcel to be active ($\mathrm{Prob}(\mathrm{S}_k = 1)$). δ is a Dirac function which is used to switch off the parcel when $\mathrm{S}_k = 0$. $\mathcal{N}(\boldsymbol{\mu}_k, \boldsymbol{\Sigma}_k)$ is a Gaussian distribution of the intensities of the kth parcel, $\boldsymbol{\mu}_k$ describing the mean and $\boldsymbol{\Sigma}_k$ describing the covariance of all the sources within that kth parcel.

In this study, we considered the "coherent" version of MEM, entitled cMEM, originally introduced in Chowdhury et al., 2013 and fully described in Chowdhury et al., 2016. The term "coherent" refers to the fact that we are using a coherent spatial prior, that is, a data driven parcellation in K parcels which is fixed along time, while the probability of being active α_k can evolve dynamically. In cMEM implementation, we also included local spatial smoothness within each parcel of the model.

Therefore, in cMEM, to initialize the spatial prior model, $\boldsymbol{\mu}_k$ is set to zero and $\boldsymbol{\Sigma}_k$ is defined as follows:

$$\boldsymbol{\Sigma}_k(t) = \eta_k(t)\boldsymbol{W}_k(\sigma)^T\boldsymbol{W}_k(\sigma) \quad \text{(A6)}$$

where $\boldsymbol{\Sigma}_k(t)$ is the source covariance of parcel k at each time sample t, $\boldsymbol{W}_k(\sigma)$ is a spatial smoothness matrix which controls the local smoothness within the parcel (σ set to 0.6; Chowdhury et al., 2013; Friston et al., 2008) and $\eta_k(t)$ is defined as 5% of the energy of minimum norm estimate (MNE) solution (Lin et al., 2006) of all the r_k sources within the parcel kth.

$$\eta_k(t) = 0.05\frac{1}{r_k}\sum\nolimits_{i \in r_k}\hat{j}^2_{\text{MNE}}(i,t) \quad \text{(A7)}$$

The MNE solution $\hat{\mathbf{j}}_{\text{MNE}}$ was calculated using:

$$\hat{\mathbf{j}}_{\text{MNE}} = \text{argmin}\left(\|\boldsymbol{m}-\mathbf{G}\mathbf{j}\|^2_{\boldsymbol{\Sigma}_d}+\lambda\|\mathbf{j}\|^2_{\boldsymbol{\Sigma}}\right) = \left(\boldsymbol{G}^T\boldsymbol{\Sigma}_d\boldsymbol{G}+\lambda\boldsymbol{\Sigma}\right)^{-1}\boldsymbol{G}^T\boldsymbol{\Sigma}_d\boldsymbol{m} \quad \text{(A8)}$$

where $\boldsymbol{\Sigma}_d$ is the inverse of the noise covariance, $\boldsymbol{\Sigma}$ is the inverse of the source covariance ($\boldsymbol{\Sigma} = \boldsymbol{I}_r$, an $r \times r$ identity matrix), and λ is a hyperparameter to regularize the inversion. Standard L-Curve method was used to estimate λ.

After the reference distribution $d\nu$ is initialized, the MEM solution is finally obtained through an optimization of a convex function obtained from the dual formulation of the maximum entropy principle (Amblard et al., 2004; Chowdhury et al., 2013, 2016).

A.2 | Depth-weighted cMEM (cMEM$_\omega$)

We are introducing a new parameter for cMEM implementation. Depth weighting within cMEM framework was first proposed and implemented by Cai et al. (2022) for functional Near InfraRed Spectroscopy 3D reconstruction. Similarly to the depth weighting strategy proposed for MNE (Lin et al., 2006), we introduced a location penalty in the source covariance by scaling it with the forward model and thus penalizing the superficial sources that exhibit larger amplitude and enhancing the contribution from deep sources. This penalization was tuned by the weighting parameter ω. Therefore, $\omega = 0.0$ refers to no depth weighting whereas increasing the value of ω would refer to more contribution from deep sources.

Therefore, in cMEM$_\omega$ depth weighting was implemented when initializing the spatial prior. The parcels are initialized using the source covariance of the parcel, $\boldsymbol{\Sigma}_k$ (Equation A6). The source covariance in Equation A6 was weighted by the forward model of each vertex, quantifying the influence of source depth, to a specific power ω. Therefore, following the method proposed and validated by Cai et al. (2022), depth weighting was added at two levels:

1. To initialize the spatial prior model, we applied depth weighting in the source covariance for each parcel, $\boldsymbol{\Sigma}_k(t)_\omega$ as:

$$\boldsymbol{\Sigma}_k(t)_\omega = \boldsymbol{\Lambda}_{r_k}\eta_k(t)_\omega\boldsymbol{W}_k(\sigma)^T\boldsymbol{W}_k(\sigma) \quad \text{(A9)}$$

where $\boldsymbol{\Lambda}_{r_k}$ is the depth weighting matrix defined as the diagonal matrix of $\left(\mathbf{G}_k{}^T\mathbf{G}_k\right)^{-\omega}$, where $\boldsymbol{G}_k$ is the gain matrix for r_k sources in parcel k.

2. For cMEM, $\eta_k(t)$ was defined as 5% of the energy of MNE solution of r_k sources within the parcel k (Equation A7). In cMEM$_\omega$, we replaced the MNE solution with the depth-weighted MNE solution. Equations A7 and A8 are modified as follows:

$$\eta_k(t)_\omega = 0.05\frac{1}{r_k}\sum_{i \in r_k}\hat{\mathbf{j}}_{\text{MNE}_\omega}(i,t)^2 \quad \text{(A10)}$$

where $\hat{\mathbf{j}}_{\text{MNE}_\omega}$ is the depth-weighted version of $\hat{\mathbf{j}}_{\text{MNE}}$ in Equation A8, where we used the diagonal of the source covariance matrix $\boldsymbol{\Sigma}$, weighted by the forward model, as follows:

$$\boldsymbol{\Sigma} = \boldsymbol{I}_r\left(\boldsymbol{G}^T\mathbf{G}\right)^{-\omega} \quad \text{(A11)}$$

In this study, we considered a fixed depth weighting factor, $\omega = 0.5$ (zero would represent no depth-weighting) for the two levels reported in Equations A9 and A11. This is different from Cai et al. (2022), where they explored different pairs of weighting factors for Equations A9 and A11 using realistic simulations of Functional Near-infrared spectroscopy data and reported the best reconstruction accuracy for $\omega = 0.3$ for Equation A9 and $\omega = 0.5$ for Equation A11. In our EEG/MEG study, $\omega = 0.5$ was chosen to be consistent with the default value used in depth-weighted MNE (MNE$_\omega$) implementation for EEG/MEG source imaging in Brainstorm (Tadel et al., 2011). We also explored ω values ranging between 0.1 and 0.9 for one set of MEG simulations and observed that higher ω values enhanced the localization of deep sources but adversely affected the localization of superficial sources. Therefore, choosing $\omega = 0.5$ appeared as a reasonable compromise.

A.3 | Wavelet-based maximum entropy on the mean (wMEM)

wMEM is another version of MEM specifically designed to localize brain oscillatory patterns. wMEM applies a discrete wavelet transformation (Daubechies wavelets) to characterize the oscillatory patterns in the data before applying the MEM solver (Lina et al., 2012). In this work, we are introducing a new parameter for wMEM implementation to allow depth weighting, resulting in the method wMEM$_\omega$ with $\omega = 0.5$. wMEM$_\omega$ method was validated using the same simulation datasets as cMEM$_\omega$ and MNE$_\omega$ for localizing epileptic spikes. More details on wMEM implementation can be found in Lina et al. (2012) and Afnan et al. (2023).

In wMEM, the time expansion of data is substituted with a time-scale representation. In terms of wavelet expansion, Equation A1 can be written as:

$$\mathbf{d}_{s,n} = \mathbf{G}\mathbf{w}_{s,n} + \mathbf{w}^{\epsilon}{}_{s,n} \quad \text{(A12)}$$

where $\mathbf{d}_{s,n}$, $\mathbf{w}_{s,n}$, and $\mathbf{w}^{\epsilon}{}_{s,n}$ are the wavelet coefficients for the data, the sources, and the measurement noise, respectively, for a particular discrete time index n and scale s ($s = 1, 2, 3, \ldots$ with $s = 0$ being the sampling scale). Depth weighting is implemented for the step when we initialize the spatial prior (as described for cMEM$_\omega$). The time-scale representation of Equations A6 and A7 are:

$$\boldsymbol{\Sigma}_k(s,n) = \eta_k(s,n)\boldsymbol{W}_k(\sigma)^T\boldsymbol{W}_k(\sigma) \tag{A13}$$

$$\eta_k(s,n) = 0.05\frac{1}{r_k}\sum_{i \in r_k}\widehat{\mathbf{j}}_{MNE}(i,s,n)^2 \tag{A14}$$

where $\boldsymbol{\Sigma}_k(s,n)$ is the source covariance of parcel k at a particular discrete time index n and scale s. $\eta_k(s,n)$ is defined as 5% of the energy of MNE solution of all the sources (r_k) within the parcel k for a particular discrete time index n and scale s. The MNE solution $\widehat{\mathbf{j}}_{MNE}$ is calculated in time-scale domain as:

$$\widehat{\mathbf{j}}_{MNE} = argmin\left(\|\mathbf{d}_{s,n} - \boldsymbol{G}\mathbf{w}_{s,n}\|^2_{\boldsymbol{\Sigma}_d} + \lambda\|\mathbf{w}_{s,n}\|^2_{\boldsymbol{\Sigma}}\right) = \left(\boldsymbol{G}^T\boldsymbol{\Sigma}_d\boldsymbol{G} + \lambda\boldsymbol{\Sigma}\right)^{-1}\boldsymbol{G}^T\boldsymbol{\Sigma}_d\mathbf{d}_{s,n} \tag{A15}$$

where $\boldsymbol{\Sigma} = \boldsymbol{I}_r$ an $r \times r$ identity matrix.

A.4 | Depth-weighted wMEM (wMEM$_\omega$)

Similar to cMEM$_\omega$, the depth weighting was applied in wMEM at two levels. First, we applied depth weighting in the source covariance for each parcel, $\boldsymbol{\Sigma}_k(s,n)_\omega$ as:

$$\boldsymbol{\Sigma}_k(s,n)_\omega = \boldsymbol{\Lambda}_{r_k}\eta_k(s,n)_\omega\boldsymbol{W}_k(\sigma)^T\boldsymbol{W}_k(\sigma) \tag{A16}$$

where $\boldsymbol{\Lambda}_{r_k}$ is the depth weighting matrix defined as the diagonal matrix of $\left(\mathbf{G}_k{}^T\mathbf{G}_k\right)^{-\omega}$, where $\boldsymbol{G}_k$ is the gain matrix for r_k sources in parcel k. Second, we defined $\eta_k(s,n)_\omega$ as 5% of the energy of the depth-weighted MNE solution, for which we modified Equation A15 by using the diagonal of the source covariance matrix $\boldsymbol{\Sigma}$, weighted by the forward model (see Equation A11: $\boldsymbol{\Sigma} = \boldsymbol{I}_r\left(\boldsymbol{G}^T\boldsymbol{G}\right)^{-\omega}$). Similar to cMEM$_\omega$, we considered a fixed depth weighting factor, $\omega = 0.5$ for wMEM$_\omega$ at the two levels described by Equations A11 and A16.